JGR Solid Earth

RESEARCH ARTICLE
10.1029/2024JB029632

Structural Controls on Megathrust Slip Behavior Inferred From a 3D, Crustal-Scale, P-Wave Velocity Model of the Alaska Peninsula Subduction Zone

T. Acquisto[1], A. Bécel[1], J. P. Canales[2], and E. Beaucé[1]

[1]Lamont-Doherty Earth Observatory of Columbia University, Palisades, NY, USA, [2]Department of Geology and Geophysics, Woods Hole Oceanographic Institution, Woods Hole, MA, USA

Key Points:

- Our 3D Vp model reveals long-wavelength crustal-scale variations in the subducting Pacific plate and overriding North American plate
- Subducting seamounts and swell, and fracture zones modulate sediment distribution, plate hydration and influence changes in slip behavior
- Variations in backstop architecture and composition contribute to variable megathrust slip behavior both along-strike and downdip

Supporting Information:

Supporting Information may be found in the online version of this article.

Correspondence to:

T. Acquisto,
acquisto@ldeo.columbia.edu

Citation:

Acquisto, T., Bécel, A., Canales, J. P., & Beaucé, E. (2024). Structural controls on megathrust slip behavior inferred from a 3D, crustal-scale, P-wave velocity model of the Alaska Peninsula subduction zone. *Journal of Geophysical Research: Solid Earth*, *129*, e2024JB029632. https://doi.org/10.1029/2024JB029632

Received 3 JUN 2024
Accepted 4 NOV 2024

Author Contributions:

Conceptualization: A. Bécel, J. P. Canales
Data curation: T. Acquisto
Formal analysis: T. Acquisto, E. Beaucé
Funding acquisition: A. Bécel, J. P. Canales
Investigation: A. Bécel, J. P. Canales
Methodology: T. Acquisto, A. Bécel, E. Beaucé
Project administration: A. Bécel
Resources: A. Bécel
Software: T. Acquisto, E. Beaucé
Supervision: A. Bécel
Validation: T. Acquisto
Visualization: T. Acquisto, E. Beaucé
Writing – original draft: T. Acquisto, A. Bécel, J. P. Canales, E. Beaucé
Writing – review & editing: T. Acquisto, A. Bécel, J. P. Canales, E. Beaucé

Abstract In subduction zones, along-strike and downdip variations in megathrust slip behavior are linked to changes in properties of the subducting and overriding plates. Although marine geophysical methods provide insights into subduction zone structures, most surveys consist of sparse 2D profiles, limiting our understanding of first-order controls. Here, we use active-source seismic data to derive a 3D crustal-scale P-wave velocity model of the Alaska Peninsula subduction zone that encompasses both plates and spans the Semidi segment and SW Kodiak asperity. Our results reveal modest variations within the incoming plate, attributed to a series of fracture zones, seamounts and their associated basement swell, collectively contributing to plate hydration. Basement swell appears to modulate the distribution and type of sediment entering the trench, likely impacting observed variations in slip behavior. The overriding plate exhibits significant heterogeneity. The updip limit and width of the dynamic backstop are similar between the SW Kodiak asperity and eastern Semidi segment, but differ significantly from the Western Semidi segment. These distinctions likely account for differences in earthquake rupture patterns and interseismic coupling among these segments. Additionally, high-velocities in the mid-lower forearc crust coincide with the location of megathrust slip during the Mw 8.2 2021 Chignik event. We interpret these velocities as intracrustal intrusions that contributed to the deep rupture of the 2021 event. Our findings suggest that the contrasting structural and material properties of both the incoming and overriding plates influence the spatially complex and semi-persistent segmentation of the megathrust offshore the Alaska Peninsula.

Plain Language Summary Differences in styles and timing of earthquakes in subduction zones are often attributed to different geometry and properties of the plate boundary fault or megathrust, including the composition and properties of the surrounding rocks. Marine geophysical data allow us to determine structural and material differences within the subducting and overriding plates that contribute to these differences, but are typically limited to two dimensions and insufficient to properly characterize the transitions between segments with different rupture patterns and plate locking. We use recently acquired active source seismic data to create a 3D model of compressional wave velocity that encompasses both plates of the Alaska Peninsula subduction zones and spans the eastern and western Semidi segments and the SW Kodiak asperity. Our results reveal links between large structures and hydration state of the subducting plate, differences in the architecture and composition of rocks belonging to the overriding plate, and observed differences in slip behavior both along and perpendicular to the margin. These results underscore the importance of using 3D data sets to extract the combination of structures and properties of both plates that contribute to observed megathrust segmentation.

1. Introduction

Slip along the interplate boundary in subduction zones, or megathrust, triggers the largest earthquakes and some of the most devastating tsunamis on Earth. Seismic slip during a large earthquake typically occurs within the frictionally unstable seismogenic zone at depths ranging from 10 to 30 km (Scholz, 1998). This unstable zone is typically flanked by conditionally stable and stable transitional zones around depths of 0–10 km updip and 30–55 km downdip, where various forms of aseismic behaviors, such as slow slip events, tectonic tremors, and creep are observed (Lay et al., 2012). In certain circumstances, however, slip during large earthquakes can nucleate or propagate into the shallow part of the megathrust, potentially triggering a very large tsunami (Fujii et al., 2011; Ito et al., 2011). Furthermore, significant along-strike variability in slip behavior is observed in the variable depth extents of large ruptures, the patchiness of interseismic locking, and the occurrence of slow earthquakes at

seismogenic depths (e.g., Nishikawa et al., 2019; Wallace et al., 2004). Understanding possible controls on both downdip and along-strike variability in megathrust slip behavior is important for better characterizing earthquake and tsunami hazards in these complex settings.

Differences in megathrust slip behavior have been related to various large-scale plate attributes including temperature along the megathrust, convergence rate, age, and dip angle of the subducting plate (Byrne et al., 1988; Hyndman et al., 1997; Oleskevich et al., 1999; Ruff & Kanamori, 1980). However, improved observations of different megathrust behaviors, especially those over short distances, imply the existence of additional structural controls alongside these typically longer-wavelength properties (e.g., French & Condit, 2019; Wang & Bilek, 2014). Proposed subducting plate controls include the thickness and lithology of subducting sediments (Ruff, 1989; Scholl et al., 2015), the degree of hydration of the subducting plate (Acquisto et al., 2022; Gase et al., 2023; Shillington et al., 2015), downgoing plate roughness (Wang & Bilek, 2014), as well as the presence of large topographic features such as seamounts (Singh et al., 2011), ridges (Bilek, 2010), and fracture zones (Chlieh et al., 2011; Robinson et al., 2006).

Geology and structures of the overriding plate are also proposed to contribute to variable megathrust slip behaviors (e.g., Collot et al., 2004; Kopp & Kukowski, 2003; Wallace et al., 2012). Geophysical methods have helped identify the important role of upper plate tectonic stresses, permeability (Wallace et al., 2012), faulting (Ramos et al., 2022), and rigidity (Bassett et al., 2016; Sallarès & Ranero, 2019) in explaining observed differences in slip behavior. These properties ultimately relate to variations in the broader geometry and strength of the older, more deformed crustal backstop, or margin framework, a body of stronger material against which actively deforming sediments typically accrete (e.g., Silver et al., 1985). At some accreting margins, the backstop is thought to be segmented into a dynamic, slowly deforming backstop located updip of a static, more rigid backstop (Kopp & Kukowski, 2003). The geometry of the static and dynamic backstops reflects the past evolution of the margin, which controls the position of splay faults and upper plate deformation, thus having a strong effect on earthquake rupture area and tsunami potential (Kopp & Kukowski, 2003; Tsuji et al., 2015; Watt & Brothers, 2020).

Our understanding of structural controls on megathrust slip behavior relies mostly on two-dimensional (2D) multichannel seismic (MCS) profiles that tend to focus on either upper plate or subducting plate controls, minimizing the potential interconnection between them. In addition, 2D studies often fail in characterizing the nature of transitions between segments of a margin that display variations in slip patterns during large earthquakes. They also cannot fully capture evidence for downdip and along-strike variations in the locking of the plate boundary. Dense networks of 2D MCS profiles can help to overcome these limitations (e.g., Flores et al., 2024); however, velocity information will remain limited and may also be contaminated by three-dimensional (3D) effects. Recent advances in 3D imaging capabilities have improved our ability to image such transitions (Arnulf et al., 2022; Bangs et al., 2015; Gase et al., 2023; Paulatto et al., 2017, 2024) and place valuable constraints on backstop geometry and the location and nature of frictional transitions along some convergent margins (Bassett et al., 2022), however the number of 3D studies remains limited.

In this study, we focus on the portion of the Alaska Peninsula subduction zone that regularly ruptures in large ($Mw > 8$) earthquakes and displays spatial differences in interseismic locking, seismicity, megathrust rupture, and slip behavior along the strike and downdip directions. Because of the very limited 2D ocean bottom seismometer (OBS) active source seismic data available in this area (Krabbenhoeft et al., 2021; Shillington et al., 2015), questions remain regarding broad structural controls on variations in megathrust slip behavior, as well as the nature of transitions between contrasting regions both along-strike and downdip. Here we present the first 3D Vp constraints on the crustal-scale architecture and properties of the Alaska subduction zone from first-arrival tomography of wide-angle OBS data, acquired as part of the Alaska Amphibious Community Seismic Experiment (AACSE; Barcheck et al., 2020). Our 3D velocity model reveals large-scale structural variations within both the incoming and overriding plates. We examine these variations in the context of the observed differences in rupture patterns of past earthquakes, locations of shallow slow slip events and postseismic slip, and changes interseismic locking.

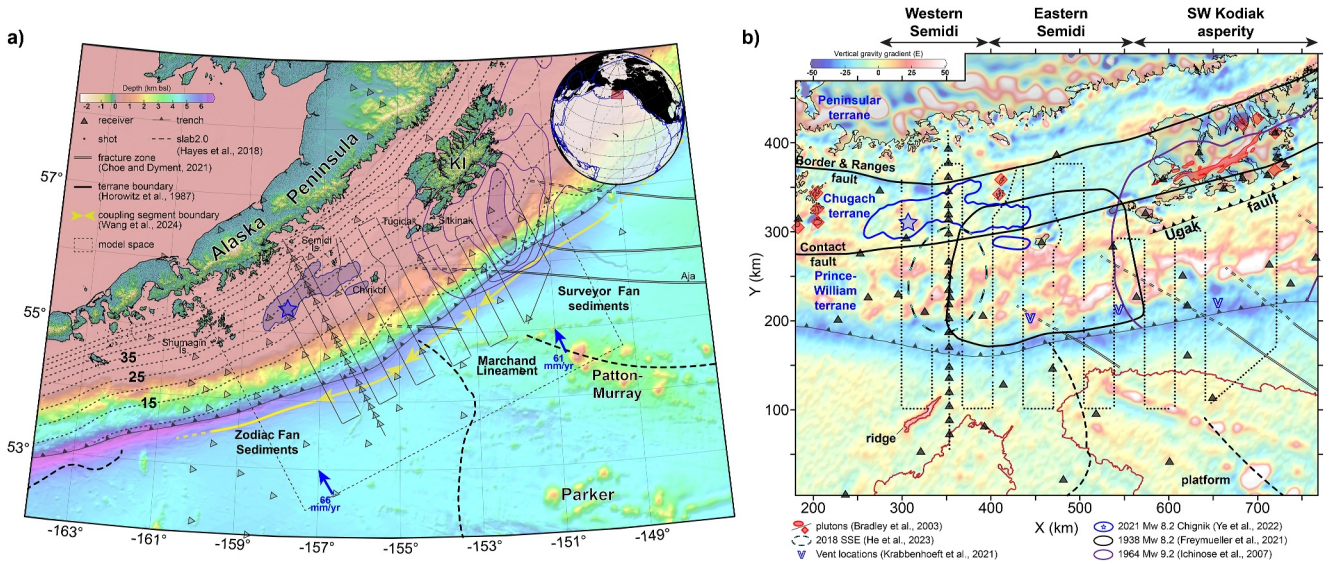

Figure 1. Study region and model area. (a) Equal area projection bathymetric map of the Alaska Peninsula subduction zone. The upper-right inset shows the location of our study region. Dashed lines on the incoming Pacific plate show the eastward and westward extents of the Zodiac (Stevenson et al., 1983) and Surveyor Fans (Zhang & Gulick, 2019), respectively. The seaward termination of the Surveyor Fan is not clear. Major seamount groups and land masses are labeled with black and white text. Blue arrows show plate convergence vectors (DeMets et al., 2010). Blue and purple curves are slip contours for the 2021 Mw 8.2 Chignik (Ye et al., 2022) and 1964 Mw 9.4 Great Alaska earthquakes (Ichinose et al., 2007). Additional markings are explained by the legend in the upper left-hand corner. (b) Vertical gravity gradient map (Sandwell et al., 2014) of our rotated Cartesian model space. Black dots and triangles are sources and receivers used during inversion. Blue and black text identify different accreted terranes separated by contacts or faults (Horowitz et al., 1989). Red lines on the incoming plate are 4.5 km bathymetric contours that highlight the Patton-Murray and Parker platforms as well as ridge structure.

2. The Alaska Peninsula Subduction Zone

Offshore of the Alaska Peninsula subduction zone, the Pacific plate subducts orthogonally beneath the North American plate at ~61–66 mm/yr (DeMets et al., 2010) and encompasses two main subduction zone segments: The Semidi segment and the southwestern Kodiak asperity (Figure 1).

The Semidi segment regularly generates great earthquakes (Davies et al., 1981; Sykes et al., 1981), with the two most recent being the 1938 Mw 8.3 earthquake and the 2021 Mw 8.2 Chignik earthquake. Slip during the 1938 Mw 8.3 earthquake was thought to span a 300-km long margin-parallel region between Kodiak and the Shumagin Islands based on the distribution of aftershock locations (Davies et al., 1981) (Figure 1a). However, a recent analysis of tide gauge data suggests that most slip during this event was concentrated in the eastern part of the segment and at depths shallower than 20 km (Freymueller et al., 2021) (Figure 1b). Conversely, multiple coseismic slip models of the 2021 Mw 8.2 Chignik event indicate that this event ruptured the western, deeper portion (20–40 km depth) of the megathrust (Elliott et al., 2022; Liu et al., 2023; Ye et al., 2022). Recent studies further highlight that the shallow portion of the western Semidi segment might be experiencing more aseismic slip (Wang et al., 2024), as evidenced by a shallow slow slip event detected in 2018 prior the Chignik event (He et al., 2023). Additionally, much of the postseismic slip following the Chignik earthquake appears to have occurred in this same area (Brooks et al., 2023). The southwestern Kodiak asperity ruptured as part of the Mw 9.2 Great Alaska earthquake in 1964 (Johnson et al., 1996). Within this asperity, the greatest amounts of slip during this earthquake were concentrated at shallow depths less than 25 km (Ichinose et al., 2007; Johnson et al., 1996; Suito & Freymueller, 2009; Suleimani & Freymueller, 2020). The 1964 rupture did not extend west of Kodiak and adjacent islands, and paleoseismic data record a history (>1,000 years) of uplift and subsidence consistent with a semi-persistent segment boundary between the Semidi segment and SW Kodiak asperity (e.g., Briggs et al., 2014; Ramos et al., 2022). In summary, our study area encompasses asperities of the 1938, 2021, and 1964 events that display dramatic along-strike variations in their depth extent and characteristics.

Coupling of the megathrust also varies along-strike, generally decreasing from NE to SW, and transitioning from a wide zone of high coupling that encompasses the shallow megathrust outboard Kodiak Island to smaller zones of coupling in the Semidi segment (Drooff & Freymueller, 2021; Elliott et al., 2022; Wang et al., 2024; Xiao

et al., 2021). The updip extent of coupling remains poorly constrained, particularly in the Semidi segment, as the forearc is largely offshore and studies utilize onshore GNSS observations. Indeed, different models with various setups of downdip coupling have been shown to explain the data equally well, with some of the models incorporating sharp boundaries along-strike (e.g., Drooff & Freymueller, 2021; Xiao et al., 2021). The observed contrasting slip behaviors between the 1938 and 2021 events, combined with recent seismic and geodetic modeling suggests the Semidi segment may be divided into two sub-segments approximately centered around the Semidi Islands: the eastern Semidi Segment that appears well-coupled from the trench down to 40 km depth and the western segment that is coupled at depth (30–40 km) but aseismic at depths <25–30 km (Wang et al., 2024). Our study area crosses 3 of these modeled segment boundaries (Figure 1b). The degree of background seismicity also varies between segments for both the incoming and overriding plates. The lowest level of seismicity occurs in the Semidi segment compared to the Kodiak asperity and neighboring Shumagin Gap (Shillington et al., 2015). The high level of seismicity within the Kodiak asperity may in part be explained by postseismic deformation following the 1964 earthquake (e.g., Doser et al., 2002).

Outboard our study area, the ∼43–51 Ma incoming Pacific plate (Malinverno et al., 2020) formed at the Pacific-Farallon ridge at intermediate spreading rates (Engebretson et al., 1984). The inherited plate fabric is oblique to the trench axis (Figure S1b in Supporting Information S1) and few faults have been imaged outboard of the trench (Clarke et al., 2024; Reece et al., 2013). Two seamount chains are seen in the bathymetry and gravity data (Figure 1, Figure S1 in Supporting Information S1): the Patton-Murray-Marchand seamount and Parker-Gilbert seamount groups along with their respective platforms (Wessel & Kroenke, 1998). The Patton-Murray seamounts and platform, or basement swell, were created when this part of the Pacific plate moved over the Cobb Hotpot (e.g., Dalrymple et al., 1987; Desonie & Duncan, 1990). Data from ODP Hole 887D show that several intermittent periods of post-shield volcanism (i.e., volcanic rejuvenation) took place for at least 16 Myr after their initial formation by the Cobb-Eickelberg Hotspot (Keller et al., 1997). Less is known about the Parker-Gilbert seamount group and the more subdued adjacent swell given the lack of age constraints and clear link to a known hotspot (Desonie & Duncan, 1990). A small ridge structure is also present in the western part of the study area (Bécel et al., 2015), which correlates spatially to a change in orientation of magnetic anomalies associated with the fossil Kula-Pacific-Farallon triple junction (Engebretson et al., 1984). This structure also marks the eastern termination of extensive bending-faulting in the outer rise (Clarke et al., 2024) where previous 2D modeling shows little to no evidence for hydration of the upper plate there (Shillington et al., 2015). A recent 3D S-wave seismic tomography study suggests the incoming plate outboard Kodiak, and to a lesser extent Semidi, is more hydrated than previously thought, though still significantly less fluid-rich than the crust outboard the Shumagin Gap (Li et al., 2024). Other prominent features include a series of fracture zones located in the eastern part of our study area that include the subducting Aja, Akak, and 56°N fracture zones (Naugler & Wageman, 1973). These and other small fracture zones have been interpreted as offsets in the magnetic anomalies (Choe & Dyment, 2021) and gravity lows (e.g., Krabbenhoeft et al., 2021). The subduction of both the Patton-Murray seamount chain and fracture zones have been proposed to contribute to earthquake segmentation between the SW Kodiak asperity and the Semidi segment (Ramos et al., 2022; von Huene et al., 2012), yet no direct evidence for the subduction of these features exists.

The positions of two prominent terrigenous sediment fans, the Zodiac Fan outboard of the Semidi segment and the Surveyor fan outboard of the SW Kodiak asperity (Ryan et al., 2012; Stevenson et al., 1983), have also been proposed to contribute to segmentation in this area (von Huene et al., 2012). The Eocene to early Oligocene Zodiac fan (250 m thick on average) overlies a thin (<10 m) pelagic layer (Creager et al., 1973); both sequences are buried under a blanket of pelagic sediments that averages 250 m in thickness (Stevenson et al., 1983). The late Miocene to Holocene Surveyor Fan covers the older pelagic sediment (Reece et al., 2011). While the Patton-Murray platform and seamounts appear to have precluded the westward transport of the distal Surveyor fan (Reece et al., 2011; Zhang & Gulick, 2019), the transition between the two fans across the incoming plate is not clearly defined. Previous 2D seismic work has shown that the thick subducted sediment layer in the western Semidi segment is over-pressured at shallow depths (Li et al., 2018) and might consolidate downdip to facilitate the formation of a large asperity that can rupture in a great earthquake.

The overriding plate consists of a series of terranes that episodically accreted to the margin starting in the early Mesozoic, increase in age and metamorphic grade landward, and are delineated by tectonic boundaries, or contacts, that approximately mirror the modern trench axis (Horowitz et al., 1989) (Figure 1). These and other prominent faults have the potential to rupture simultaneously with the megathrust, may impact fluid transport, and

accommodate exhumation and strain partitioning (Haeussler et al., 2015; Ramos et al., 2022; von Huene et al., 2021). From north to south, this series of terranes includes the highly metamorphosed Jurassic-Triassic accretionary complexes of the Alaska Peninsula terrane, the Cretaceous mélange and deep-water turbidite sequences of the Chugach terrane, followed by the Paleogene-Neogene turbidites and shelf strata of the actively accreting Prince William terrane (Bruns et al., 1987; Fuis et al., 2008; Horowitz et al., 1989). Both the Border Ranges fault separating the Peninsula and Chugach terranes, and the Contact fault separating the Chugach and Prince William terranes are observed on Kodiak Island (Figure 1b), where outcrops of the Paleocene Kodiak batholith and slightly older basaltic trenchward belt (both belonging to the Sanak-Baranof belt) appear to have "stitched together" the different accretionary terranes (Farris & Paterson, 2009; Moore et al., 1983). Geochronological and geochemical studies suggest that these intrusive bodies have a complex petrological origin of oblique ridge subduction and possible left-lateral displacement along the Contact fault (Farris, 2010). Recent studies from the AACSE show that the thickness of the overriding crust likely increases west of Kodiak Island (Li et al., 2024) alongside an overall steepening of the downgoing slab and trench-parallel shortening of the margin (Figure S2b in Supporting Information S1). While the offshore extensions of these terrane boundaries have been mapped using gravity and magnetic data (Horowitz et al., 1989; Mankhemthong et al., 2013), precise interpretations are limited to 2D profiles west of Kodiak Island, and only map the Contact fault in the Shumagin gap (e.g., Shillington et al., 2022).

Across the margin, von Huene et al. (2021) and Krabbenhoeft et al. (2021) have identified backstop splay fault zones in the accretionary wedge, suggested to be tsunamigenic structures that approximate the updip limit of the seismogenic zone. Evidence for fluid vents and mounds between the central SW Kodiak asperity and the eastern Semidi segment (east of a 2018 slow slip event; He et al., 2023) (Figure 1b) may indicate the accumulation and release of fluids along the shallow megathrust and splays is non-uniform (Suess et al., 1998; von Huene et al., 2021); however, constraints on the hydrogeology of the outermost forearc and accretionary wedge are limited as structural and velocity information derived from MCS profiles remains sparse (Krabbenhoeft et al., 2021; von Huene et al., 2015). Recent analyses by Ramos et al. (2022) offshore Kodiak Island image the Kodiak Shelf and Albatross Banks fault zones. They observe significant Holocene uplift that indicates a higher tsunamigenic hazard along the Ugak and other faults just off the southern shore of Kodiak Island compared to the other splay faults imaged farther seaward. More recent 3D passive-source studies using the AACSE earthquake catalog to provide new constraints on slab and overriding plate velocities, implying greater, non-uniform hydration of the incoming slab and overriding crust outboard the Semidi segment and SW Kodiak asperity than previously thought (e.g., Gou et al., 2022; Li et al., 2024). Higher-resolution results show that hydration may be restricted to the plate interface beneath a relatively dry overriding crust in the SW Kodiak asperity and eastern Semidi segment; however, resolution in the upper 10–15 km of the overriding plate is limited, particularly within the Prince William terrane (Wang et al., 2024). Moreover, other variations in forearc structure may be inferred from gravity anomalies, for example, beneath Kodiak Island where elevated values are representative of rocks that intruded the Chugach terrane (Horowitz et al., 1989). Kodiak Island is flanked on either side by gravity lows (Figure S1a in Supporting Information S1), which to the east has been interpreted alongside low seismic velocities and layered reflections as evidence for underplating (Ye et al., 1997). The western gravity low is collocated with a large sedimentary basin (Figure S2 in Supporting Information S1) and has also been suspected to result from underplated low-velocity rocks (Ramos et al., 2022), though this has yet to be confirmed. Therefore, observational links between overriding plate structure, terrane composition, and megathrust slip behavior remain limited offshore the Alaska Peninsula. To better understand the role of the overriding and downgoing plates in controlling the along-strike and downdip variations, we integrate interpretations of our preferred 3D Vp model with previous observations and compare our results with more recent 3D passive-source studies.

3. Data and Methods

3.1. Active-Source Seismic Data

To create a 3D crustal-scale, single-layer, P-wave velocity model encompassing the incoming and overriding plates of the Alaska subduction zone, we combine two active-source seismic data sets acquired in this area (Figure 1). The main 3D data set was acquired during *R/V Marcus G. Langseth* cruise MGL1903 in June 2019 as part of the AACSE (Barcheck et al., 2020). We supplement these data with a 2D OBS profile, AL03, acquired during *R/V Marcus G. Langseth* cruise MGL1110 in July–August 2011 as part of the Alaska Langseth Experiment to Understand the MegaThrust (ALEUT) (Shillington et al., 2015).

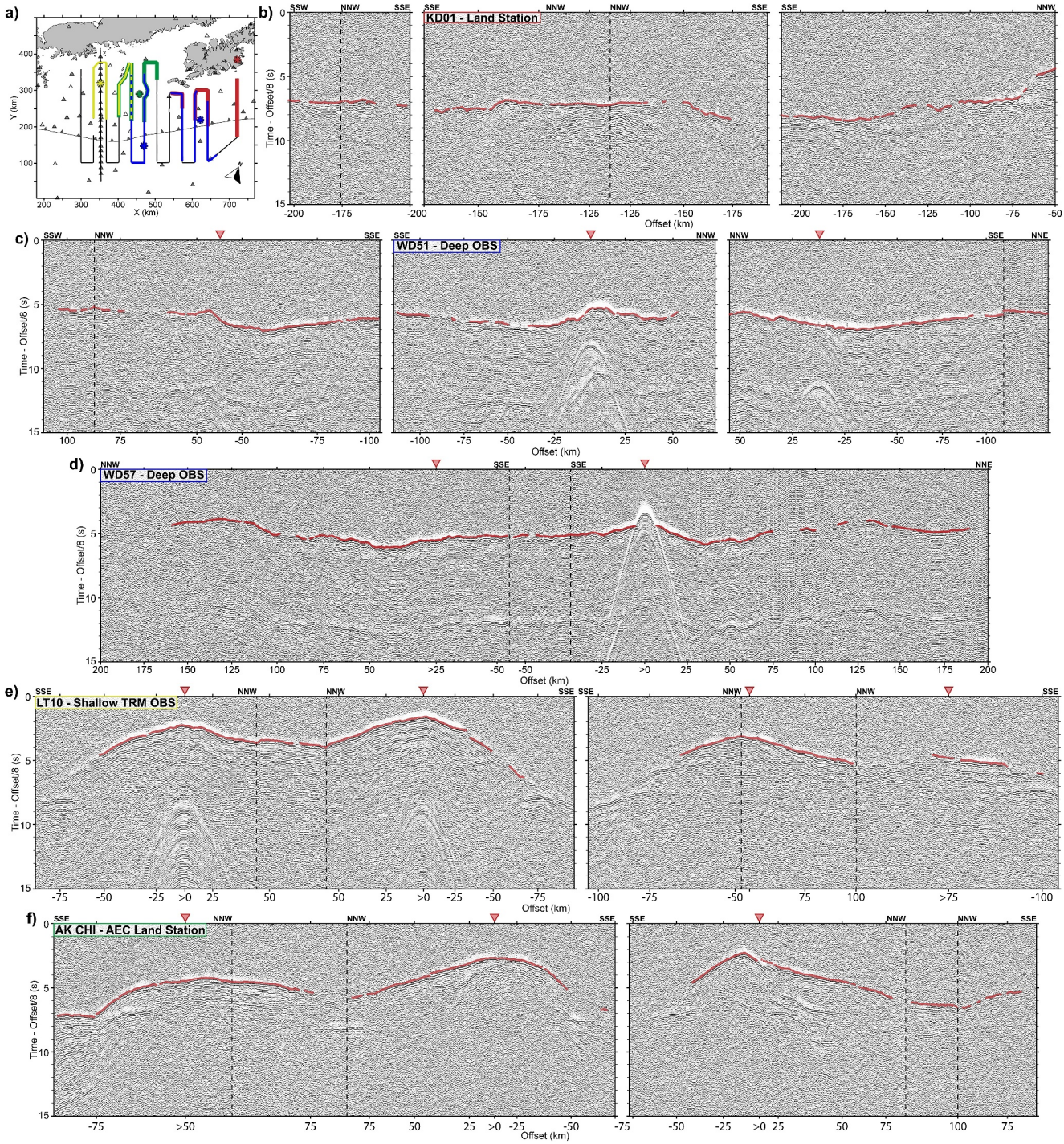

Figure 2. Example of onshore and offshore OBS common-receiver gathers with traveltime picks in red. The data are reduced at 8 km/s and automatic gain control has been applied. (a) Map of the model space identifying each source-receiver pair plotted in (b)–(f). Dashed lines mark turns in the shot-lines and red triangles show corresponding receiver locations projected across *X*. Offset is negative when sources are below (in *Y*) their corresponding receiver. Note the far-offset refracted (e.g., >15 km on OBS WD57) arrivals and strong plate-boundary and Moho reflections below the refractions (e.g., offsets around −75 km at ∼8–9 s for OBS LT10).

The AACSE instrument deployment consisted of 30 onshore and 75 offshore broadband seismometers and also leverages the presence of nearby stations belonging to the EarthScope Transportable Array (TA) and the Alaska Earthquake Center (AEC). Sources during cruise MGL1903 were created using a 6,600 in^3 airgun array that was towed at 12 m deep and fired every 400 m for a total of 7,821 shots. This corresponded to 12 trench-perpendicular

shot profiles that were between 160 and 275 km in length each connected orthogonally by shorter ∼34 km-long profiles. During this survey, a 4 km-long hydrophone steamer was towed at 12 m depth for the first seven trench-perpendicular profiles in the northeastern part of our survey area (Barcheck et al., 2020). The data were low fold (5), but produced high-quality images (Bécel et al., 2019). The 2D trench-perpendicular line AL03 consisted of 21 short-period OBSs nominally spaced 15 km apart along a coincident 365 km-long shot line. The source size and tow-depth were the same as in MGL1903, but with a shot spacing of 310 m (Figure 1b).

Of the 105 deployed AACSE instruments, 72 were operating during MGL1903. To maximize ray coverage, we incorporated vertical-component data from TA and AEC stations located on the Alaska Peninsula, Kodiak Island (S19K), and the smaller Sitkinak (SII), Chirikof (CHI), and Shumagin Islands (CHN). All but one of the AL03 OBS successfully recorded 1,167 shots during MGL1110. Pre-processing and first-arrival picking were performed using Shearwater's Reveal seismic processing software. Prior to interpretation, we applied a bandpass filter with cut-off frequencies at 5 and 15 Hz, predictive deconvolution with a 100 ms gap and 1,200 ms operator length, and linear moveout to help identify coherent refracted arrivals. Shot energy recorded on the AACSE hydrophone component was very weak, thus we opted to interpret on the vertical component (BHZ) instead. Figure 2 shows 3D receiver gathers and interpreted first-arrivals for different instruments throughout the model space. For AL03, we used information recorded by the hydrophones.

We interpreted 42,103 first-arrivals out of 609,915 available traces with 32,024 (76%) coming from 37 of the AACSE instruments, 3,541 (8%) from the 3 AEC instruments, and 6,538 (16%) from the 20 instruments in the AL03 data set. Pick uncertainties were tied to offset in the same way for both onshore and offshore instruments and range between 50 and 175 ms for source-receiver offsets between 5 and 200 km. These errors are similar to values adopted in other 3D studies (e.g., Bassett et al., 2022) and slightly larger than those reported in similar 2D studies (e.g., Shillington et al., 2015, 2022). For the data modeling and inversion, we opted to restrict to source-receiver offsets between 5 and 200 km (representing 37,251 or 88% of the picks) and selected picks from every 10th shot for the MGL1903 data and every 14th shot for the MGL1110 data, resulting in 3,507 total picks used. Given the relatively large instrument spacing, a greater density of picks from, for example, every 5th shot only serves to increase computation times with minimal changes to the long-wavelength velocity structure.

3.2. Inversion Method and Modeling Approach

We first rotated all latitude/longitude information into a 2D Cartesian grid such that the trench-perpendicular shot lines were parallel to the *Y*-axis. The seafloor was created by slightly smoothing the Global Multi-Resolution Topography data set (v4.0; Ryan et al., 2009) and then rounding to our minimum grid spacing in *Z* (0.5 km).

We used the 3D traveltime tomography code Tomo3D (Meléndez et al., 2015) for the forward (raytracing) and inverse modeling steps, which are both parallelized to dramatically reduce the computation time. All computations were performed on the Columbia University Ginsburg cluster using 10 CPUs with 16 cores each, with computational resources being distributed to 10 out of the 60 receivers at a time. The raytracing scheme employed a combination of the shortest path and bending methods (Moser, 1991; Moser et al., 1992) and used a sheared mesh that can accommodate variable spacing between nodes (Korenaga et al., 2000). The inversion algorithm consisted of iterative regularized inversions in a least squares sense that minimized a normalized combination of the data residuals and smoothing constraints. Smoothing matrices were created using correlation lengths that varied across nodes and damping was applied when model perturbations exceed a certain percentage which we set to be 5% (Korenaga et al., 2000; Melendéz et al., 2015).

Because the inverse problem is ill-posed, strong regularization is needed to minimize non-uniqueness (e.g., Van Avendonk et al., 1998). Moreover, the sparseness of our data set underscores the importance of providing an accurate starting model. Thus, we first inverted the AL03 data in 2D (*Y*-direction) and tied the result to the trench axis to construct the 3D starting model. The starting model for the 2D inversion was created using 1D averages from Shillington et al. (2015). After 10 iterations, the initial Chi-square, or sum of the squared error-weighted traveltime residuals, was reduced from ∼76 to ∼1 (corresponding to an average RMS misfit reduction from 660 to 68 ms). To avoid a strong, persistent imprint of features specific to this area elsewhere in the 3D model, we smoothed the 2D result using a 12.5 km by 1.5 km anisotropic Gaussian kernel. The extra care taken to build the starting model helped to reduce the initial Chi-square and give the initial residuals a more normal distribution (Figure 3a).

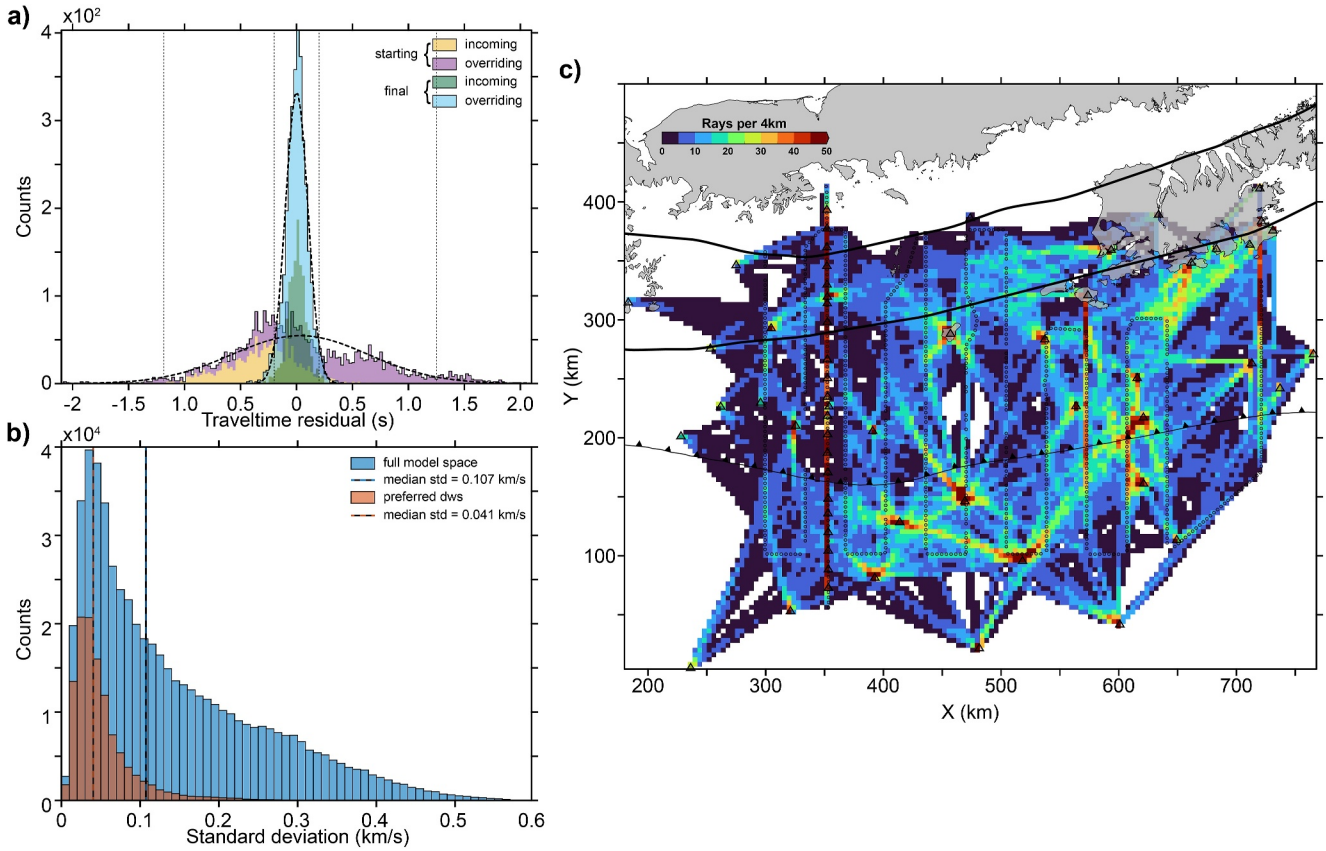

Figure 3. Inversion statistics and ray coverage. (a) Histogram of starting and final residuals color coded by the position of turning points in the incoming and overriding plates, seaward or landward of the trench, respectively. Dashed lines are Gaussian fits. (b) Histogram of ensemble standard deviations for the entire model space and within the preferred DWS. (c) Map of depth-integrated ray coverage within 4 km × 4 km nodes equal to the model grid spacing in *X* and *Y*.

Given the large spacing between available instruments (30–50 km), long-wavelength target resolution, and computational limitations, we opted for a grid spacing of 4 km in *X* and *Y* and a variable spacing in *Z* starting from 0.5 at the seafloor and increasing linearly to 1.5 km down to 35 km below the seafloor. We set correlation lengths to increase linearly in a similar manner to the grid spacing in *Z*. For *X* and *Y*, correlation lengths increase from 10 to 15 km and for *Z*, from 1 to 2 km. We tested different values for grid spacings, correlation lengths, and other important parameters during the 2D modeling. A full description of our preferred values can be found in Table S1 of the Supporting Information S1. Following, we performed iterative regularized 3D inversions, making sure to use the same modeling parameters optimized during the 2D inversions. Initially, the solution converged to a Chi-square of ∼1.3. We then removed pick outliers based on their final traveltime misfit, reducing the number of picks to 3,334. After 15 iterations, the initial Chi-square reduced from ∼49 (RMS misfit of 619 ms) to ∼1 (an RMS misfit of 86 ms), indicating that most of the final traveltime misfits lie within our prescribed pick uncertainties (Figure 3a). To avoid over-fitting, we choose the 12th iteration with a Chi-square of 1.2 (average RMS traveltime misfit of 95 ms) to be our preferred model.

3.3. Estimates of Velocity Uncertainty and Model Resolution

To assess the impact of the starting model on our final results and provide a relative measure of velocity uncertainty, we performed a Monte Carlo analysis (e.g., Canales et al., 2017; Korenaga et al., 2000; Shillington et al., 2015) by creating 50 perturbed starting models, adding random Gaussian noise to the traveltime data (constrained by the pick errors), and inverting the data with the same forward calculation and regularization parameters. The new starting models were created by randomly assigning perturbation values up to ±10% at the top and bottom of our sheared 3D mesh and linearly interpolating in between. A full description of these values is presented in Figure S3 of the Supporting Information S1. Each of the perturbed models reached a Chi-square of

~1.2 within 12–15 iterations. Therefore, we defined our preferred final model as the average across all the Monte Carlo ensembles and the preferred derivative weight sum (DWS) as overlapping voxels from each ensemble where the DWS is greater than zero. The mean standard deviation of the model ensembles is 0.041 km/s within the preferred DWS and 0.107 km/s within the entire model (Figure 3b), indicating a relatively weak dependence on the starting model in areas with the highest relative ray coverage (Figure 3c).

We also assess the resolving power of our data and modeling approach by performing two checkerboard tests. We follow the approach of Zelt (1998), adding 10% sinusoidal velocity perturbations sized 100 km in X and Y, and 10 km in Z. For the second test, we shifted the anomalies in depth by 5 km. The results of these tests are summarized in Figure S4 of the Supporting Information S1, which shows good recovery of long-wavelength velocity structure down to 20 km depth through most of the regions with ray coverage. Anomaly recovery within the overriding plate is poor just landward of the trench between $X = 400$–500 km and $Z = 5$–15 km, but improves at greater depths (Figures S4d and S4f in Supporting Information S1).

Finally, we relocated 969 earthquakes using P- and S-wave first arrival picks from the AACSE catalog (see Data Availability Statement), our preferred velocity model, and the location software NonLinLoc (Lomax et al., 2000). To solve for the earthquake hypocenters, we used the efficient, global search algorithm Oct-tree to maximize the equal differential time (EDT in NonLinLoc) likelihood using pre-computed traveltime-tables. We computed the traveltimes using the Eikonal equation solver PyKonal (White et al., 2020; see Data Availability Statement). An S-wave model was calculated using an empirical relationship for Vp/Vs determined for common sedimentary and crystalline rocks (Brocher, 2005). We also repeated the process but using the initial model, which shows a 30% reduction in the mean RMS traveltime misfit between events relocated using the initial and preferred Vp models (Figure S5 in Supporting Information S1).

4. Results

Figures 4 and 5 show vertical slices in X and Y, respectively, and Figure 6 shows uniform depth slices each taken through our preferred 3D P-wave velocity model. All velocity images are masked by the 0.1 km/s standard deviation contour. Figures S6–S11 in Supporting Information S1 present additional velocity slices, including those shown in Figures 4 and 5, as well as their equivalent standard deviation images. Figure S12 in Supporting Information S1 is the standard deviation equivalent to Figure 6. All standard deviation images are plotted with an additional 0.041 km/s white contour, which is the mean standard deviation within our preferred DWS.

The highest density of modeled rays (Figure 3c) is observed in the incoming plate within ~100–125 km of the trench (between $X = 340$–650 km) as well as seaward of Kodiak Island and in the eastern Semidi segment (between $X = 550$–650 km). Shallow coverage is generally localized along the 2D trench-normal shot lines, whereas deeper rays exhibit greater azimuthal diversity. Ray coverage typically bottoms out at a depth of around 25 km seaward of the trench and down to 30 km depth landward of the trench. Thus, our model resolves long-wavelength velocity structure within the overriding accretionary terranes with resolution down into the crust and upper ~5–10 km of mantle of the Pacific plate everywhere (e.g., Figures 4 and 5).

4.1. Incoming Pacific Plate

Figure 7 shows residual gravity anomaly data (Bassett & Watts, 2015a) and total sediment thickness (Clarke et al., 2024) alongside lower crustal (3.5–6.0 km below the basement) and upper mantle vertical velocity (0.5–5.5 km below the Moho) averages and selected 1D averages of the incoming plate. Standard deviation plots for the crustal and mantle averages are shown in Figure S13 of the Supporting Information S1. Figure 8 shows post-stack time migrated MCS images of the incoming plate outboard the SW Kodiak asperity and the eastern Semidi segment that highlight the extent of the seamounts and platform. We computed the depth to oceanic basement by slightly smoothing sediment thickness values computed via natural neighbor interpolation of the data presented by Clarke et al. (2024). The Moho discontinuity was taken by assuming a 6.5 km-thick oceanic crust everywhere (e.g., Christeson et al., 2019). In the incoming plate, we recover high vertical velocity gradients expected in the subducting upper crust. Outboard Kodiak Island, sediment cover and infill add up to ~2.5 km thick near the trench, with bulk cover thinning to less than 0–0.25 km atop the platform and seamounts. Near-trench infill pinches out to <0.5 km where the Marchand seamounts approach the trench, but rebounds to similar levels outboard the Semidi segment (Li et al., 2018) (Figures 7b and 8). The trench fill west of the platform is restricted to a smaller region outboard the trench, which is also apparent in the bathymetry data (e.g., Figure 5a). Bulk

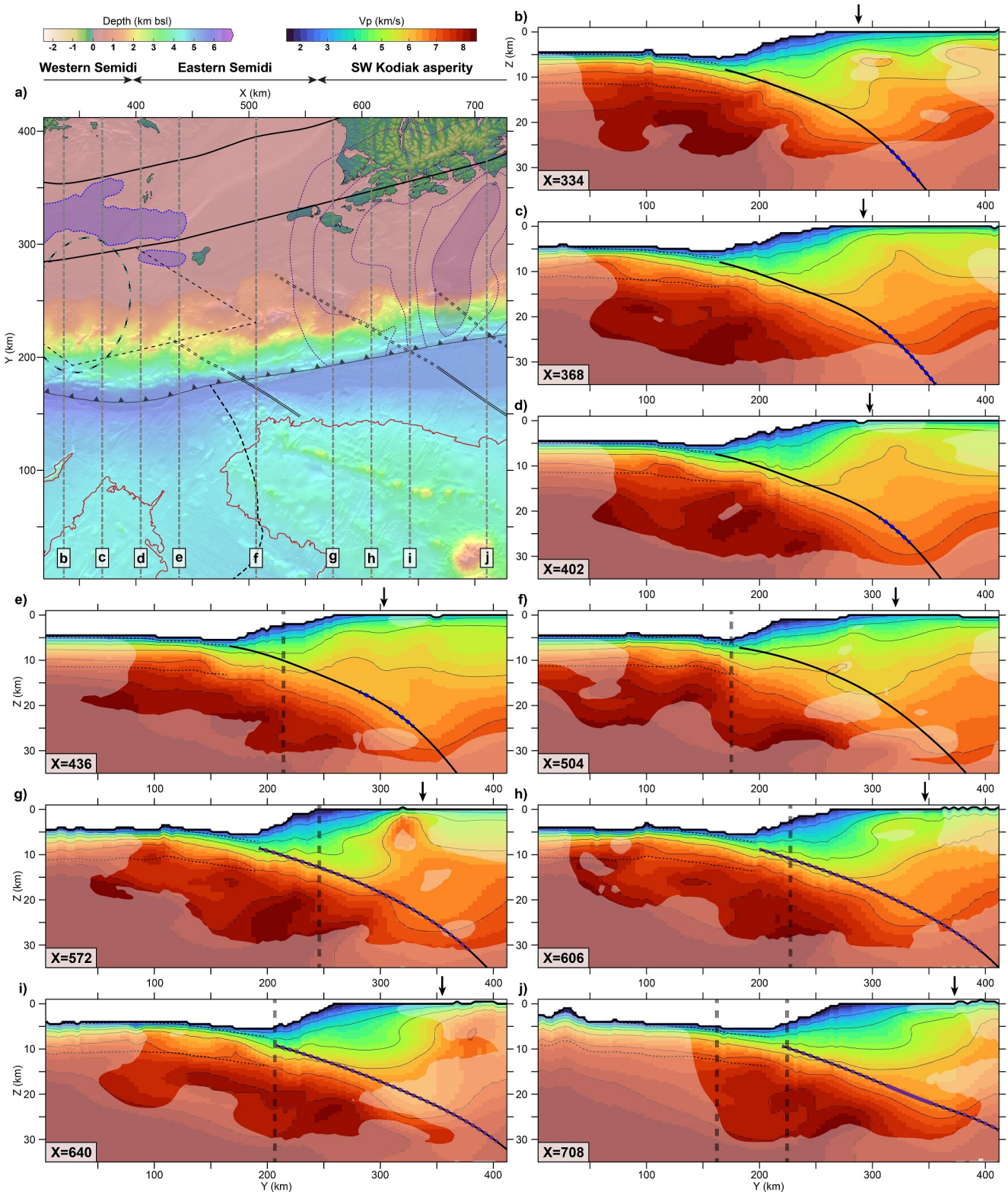

Figure 4.

sediment cover is on average thicker in the region encompassing the Zodiac Fan compared to the edge of the Surveyor Fan sediments sampled in our study area (Clarke et al., 2024).

Ray coverage is the densest within the incoming lower crust and upper mantle, with good coverage out to 80–100 km seaward of the trench (Figure 3c). Ray paths are more azimuthally diverse within ∼75 km of the trench and between X = 375–650 km. Throughout most of the incoming crust and upper mantle, we observe modest velocity variations 50–100 km in wavelength (e.g., Figures 6 and 7), highlighting a greater heterogeneity of the incoming plate than can be inferred between sparse 2D profiles (e.g., Krabbenhoeft et al., 2021; Shillington et al., 2015). Average lower crustal values range between 6.75 and 7.75 km/s while average upper mantle values fall between 7.25 and 8.5 km/s. Shallow depth slices reveal locally elevated lower-crustal velocities just southeast of the Cobb-Eickelberg platform and Marchand Seamounts as well as adjacent to the ridge structure located around X = 300 km (Figure 6b) that are also seen in 1D averages (Figure 7e). Otherwise, beneath the Marchand seamounts, within the platform, and around the fracture zones to the northeast, velocities in the crust and mantle appear slightly reduced (<7 and <8 km/s, respectively) compared to normal values from global averages (Carlson & Miller, 2003; Grevemeyer et al., 2018). We observe similar velocity reductions outboard the Semidi segment, both near the trench (X = 380–470 km) and farther seaward between X = 350–420 km and Y = 80–120 km; however, these velocity reductions appear less extensive than those seen outboard the SW Kodiak asperity (Figure 7c). Indeed, 1D averages taken atop the platform east of the Marchand lineament are typically slower compared to this taken west of the seamounts (Figure 7e).

4.2. Overriding North American Plate

Figure 9 shows velocities taken along the slab2.0 surface as well as thickness maps between the 5 and 6 km/s isovelocity contours and the slab surface. Figures 10a and 10b shows Vp slices taken coincident to ALEUT lines 2 and 3 with interpretations of the depth-migrated sections of Kuehn (2019) overlain on top. Additional comparisons are shown in Figure S16 of the Supporting Information S1. Within the overriding plate and along the slab surface, we observe velocity variations 50–100 km in size (Figures 4–6 and 9a). These variations are more subdued within the soft sediments of the shallow outer wedge (down to the 3–4 km/s contours). This is especially true between X = 475–525 km where resolution is locally poor (Figure 3c, Figures S10 and S11 in Supporting Information S1). The velocity gradients around the slab2.0 surface in this region appear more linear with depth compared to surrounding areas (Figure 5d), though ray coverage and resolution improve just landward (e.g., Figure 3, Figures S4 and S7 in Supporting Information S1). In the upper 5–10 km below the seafloor, we see locally reduced velocities that coincide with the presence of multiple known sedimentary basins (Figures 6a and 10b) that can reach more than 4–5 km depth below seafloor (e.g., Fisher, 1979; Horowitz et al., 1989).

Shallow depth slices also highlight the presence of multiple high-velocity zones. The most striking ones are the wide bodies imaged beneath southern Kodiak and the Trinity Islands (Sitkinak and Tugidak; Figure 1a) to the southwest that reach wave speeds >6 km/s within 5 km of the seafloor and peak at >7 km/s between 5 and 10 km depth (Figures 4g, 6a, and 6b). The anomaly beneath the Trinity Islands (X = 525–575 km) is ∼30–40 km wide, and appears connected to a similar anomaly just to the north that is confined to greater depths between 10 and 20 km (Figures 5a, 6b, and 6c, and Figures S8a–S8d in Supporting Information S1). The Kodiak Island anomaly is broad (>100 km wide) and trends in NE-SW (Figure 6b), mirroring outcrops of the Kodiak batholith on land (Farris, 2010; Horowitz et al., 1989) (Figure 1b). In the eastern Semidi segment, wavespeeds appear locally elevated in the Prince William terrane south-southeast of Chirikof Island (between X = 400–500 km) and in the Chugach terrane south-southwest of the Semidi Islands (around X = 410 km); however, they do not exceed 6–6.5 km/s (Figures 5c and 6b). Another large high-velocity anomaly appears partially imaged in the Chugach terrane between X = 250–315 km. This feature coincides with a downward deflection of the subducting slab (Figures 5b and 5c), the westernmost portion of the 2021 Mw 8.2 Chignik rupture area where the earthquake

Figure 4. X-slices taken through the preferred P-wave velocity model. (a) Bathymetric map showing velocity slice locations (gray dashed lines). The thin dashed rhombus is the area of afterslip following the 2021 Chignik event (Brooks et al., 2023). Other markings are the same as in Figure 1b. (b–j) P-wave velocity with transparent mask covering areas with a standard deviation exceeding 100 m/s. Solid black lines are velocity contours at 1 km/s intervals; vertical dashed lines show fracture zone intersections (Choe & Dyment, 2021); thin dashed lines in the incoming plate are the top of the oceanic crust and Moho; solid black line is Slab2.0 (Hayes et al., 2018); and dashed blue and purple lines are rupture areas for the 2021 Chignik and 1964 great earthquakes (plotted at 2 m slip contour intervals) (Ichinose et al., 2007; Ye et al., 2022). Black arrows mark the location of the Contact Fault (Horowitz et al., 1989).

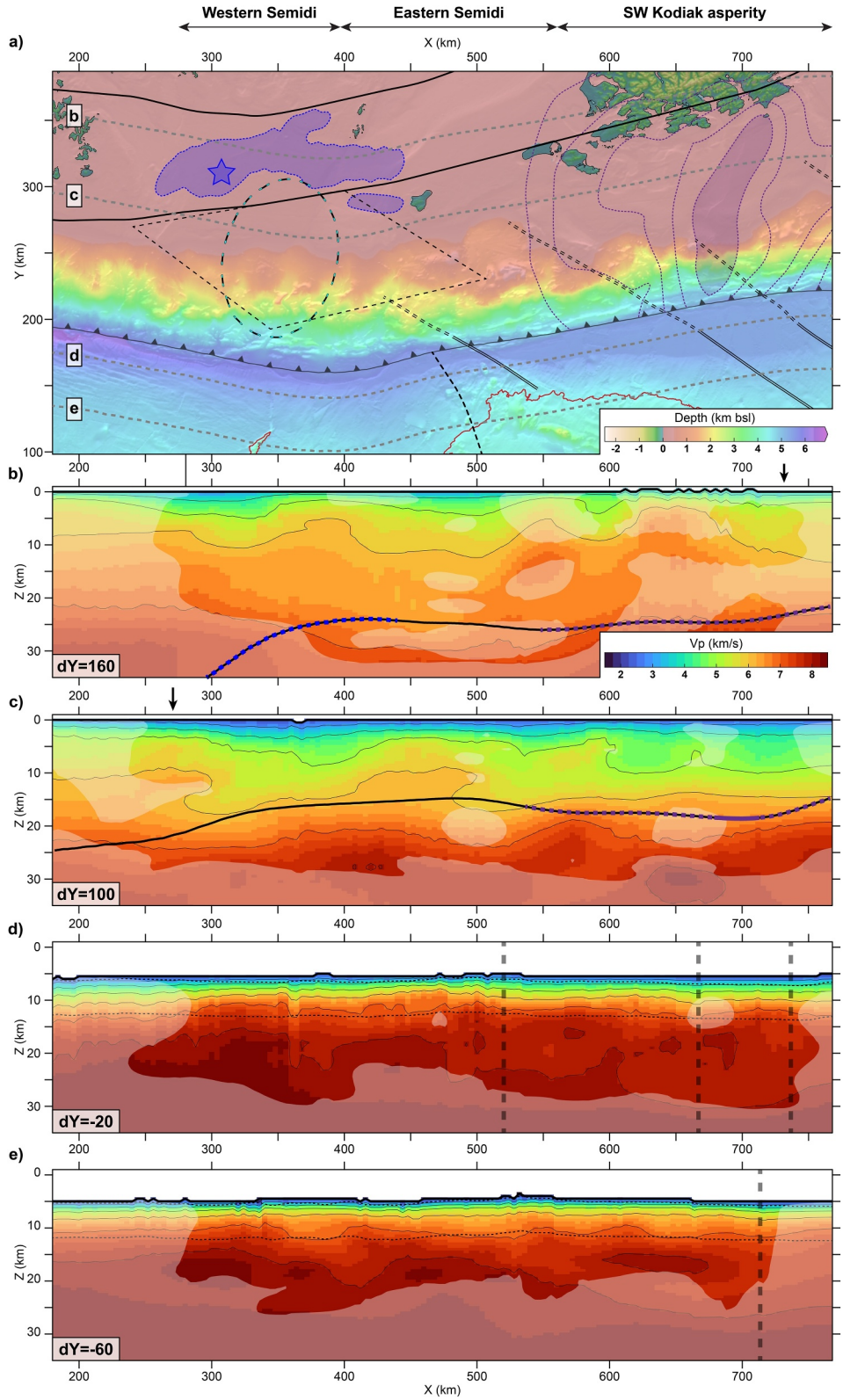

Figure 5. *Y*-slices with respect to the trench axis taken through the preferred P-wave velocity model. All other markings are the same as in Figure 4.

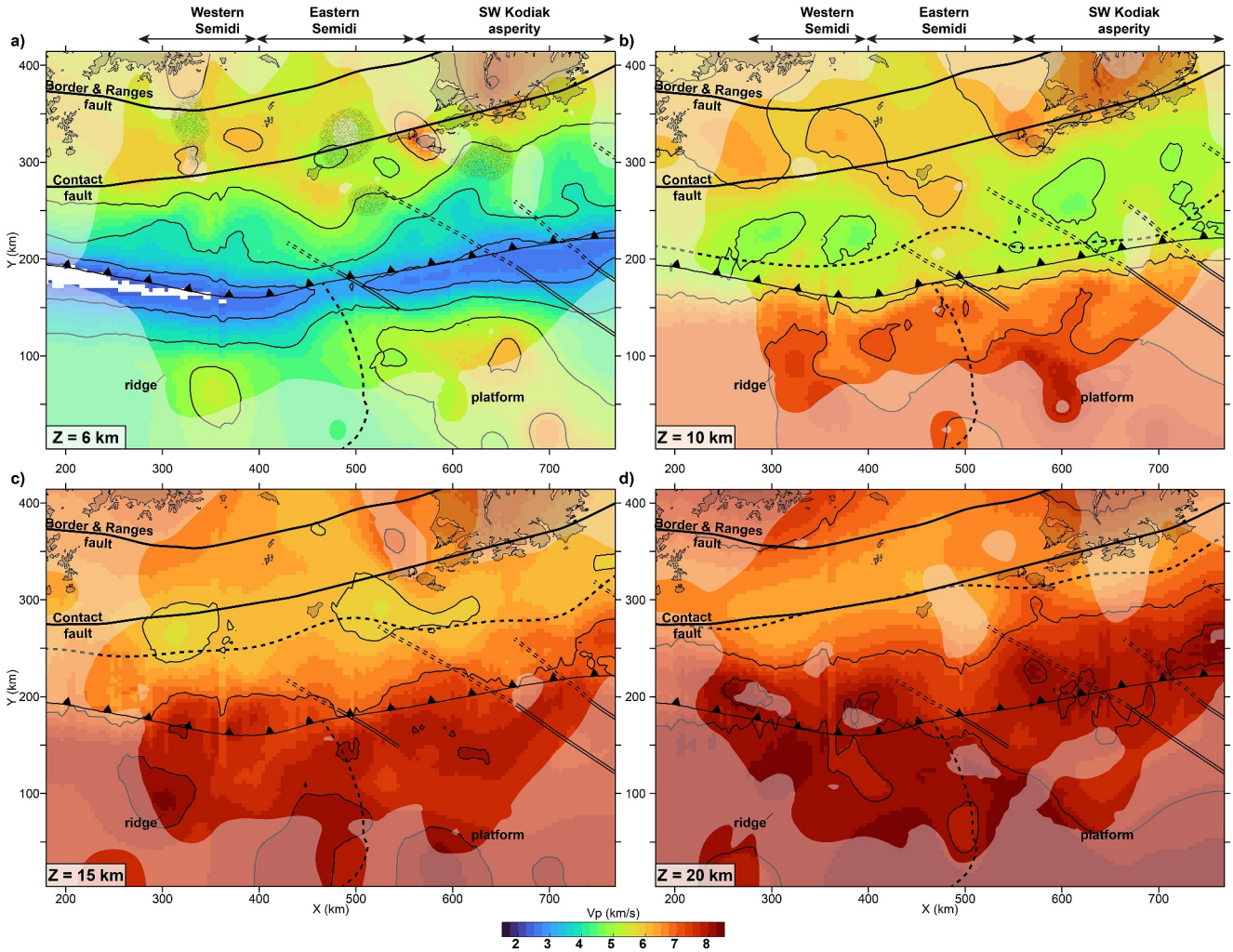

Figure 6. *Z*-slices (in km below sealevel) taken through the preferred P-wave velocity model. Dashed lines in (b)–(d) on the overriding plate shows the corresponding Slab2.0 depth contour, or intersection. Stippled areas in (a) mark the extents of known sedimentary basins from Fisher (1979) and Horowitz et al. (1989). Other markings are the same as in Figure 1b.

nucleated (Ye et al., 2022; Figure 1b), and a strong positive magnetic anomaly (Figure S1b in Supporting Information S1).

Following a similar methodology as in Bassett et al. (2022), we take the 5 km/s contour to approximate the transition between softer accretionary sediments and the crustal backstop (or margin framework). Bassett et al. (2022) define the updip limit of the crustal backstop to be where the thickness between the 5 km/s velocity isocontour and the slab surface reaches 2 km. Using the same proxy, we observe a crustal backstop (white dashed line in Figure 9b) that extends between 20 and 75 km landward of the trench. The distance between the trench and upper backstop limit is narrower on average outboard Kodiak Island (~35 km) and transitions (between $X = 570$–610 km) to ~50–75 km on average in the Semidi Segment. This transition just southwest of the Trinity Islands coincides with a sharp increase in the width between the outer slope break and the trench from 40 to 50 km outboard Kodiak Island to 60–70 km along the Semidi segment (Figure 1a) as well as the westward retreat of the crustal backstop (Figure 9b).

We further constrain different segments of the forearc by identifying where different iso-velocity contours begin to trend vertical to sub-vertical (Figures 9b and 9c and black arrows in Figure 4). Using the 5 km/s iso-velocity contour, we define the first boundary (thick black line in Figure 9b) as approximating the subsurface transition between actively deforming dynamic backstop and more rigid static backstop all within the more consolidated

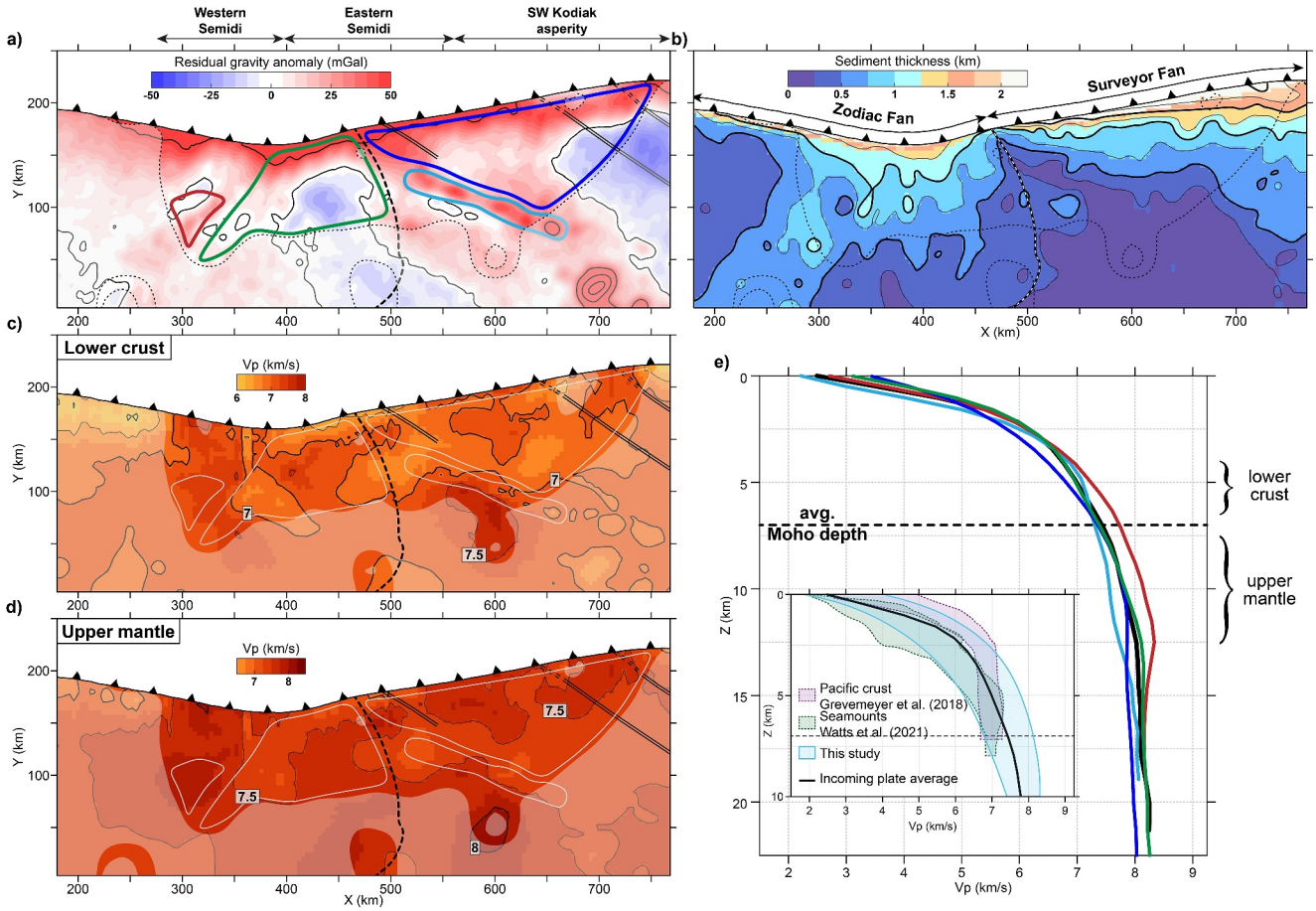

Figure 7. Velocity structure of the incoming lower crust and upper mantle. (a–d) Maps of the incoming plate showing residual gravity anomaly (Bassett & Watts, 2015a), bulk sediment thickness (Clarke et al., 2024), average Vp in the lower crust, and average Vp in the upper mantle, respectively. Other markings are the same as in Figure 1b. (e) 1D averages taken within the enclosed areas plotted in (a) taken outboard the SW Kodiak (blue and light blue), eastern (green), and western (red) Semidi segments. Inset shows the average incoming plate Vp plotted on top of tomographic averages for typical Pacific crust and other seamounts.

margin framework (e.g., Kopp & Kukowski, 2003; Tsuji et al., 2015). In the western Semidi segment, this boundary closely follows the 500 m bathymetric contour (red line in Figure 9b) between $X = 250$–400 km, but becomes more diffuse along with a slight rotation in the strike of the trench axis. The boundary is identified again starting around $X = 550$ km, and, rather than similarly narrowing to follow the outer slope break as in the western Semidi segment, it rapidly extends landward to within 20–30 km of the southern Kodiak Island shoreline (or to 100–120 km from the trench; Figure 9b). In a similar manner, we use 6 km/s iso-velocity contour to estimate the location of the Contact Fault underground (Figure 9c) (e.g., Fuis et al., 2008; Shillington et al., 2022) as we expect elevated velocities in the Chugach terranes given the higher metamorphic grade and greater abundance of intrusions compared to the Prince William terrane (Fuis et al., 2008; Horowitz et al., 1989; Moore et al., 1983; Shillington et al., 2022). Our interpretation of the Contact Fault beneath Kodiak Island follows closely where it outcrops on the surface and then wraps around the Trinity Islands before rapidly deflecting trenchward just southeast of Chirikof Island ($X = 475$ km). The Contact Fault proxy becomes more diffuse between $X = 400$–500 km within the eastern Semidi segment due to a slight local reduction in velocity in the Chugach terrane at all depths (e.g., Figures 5b, 6b, and 6c). Contact Fault proxy then transition again as a sharp boundary, closely following previous interpretations of the fault outcrop and bounding the southern extent of the 2021 Mw 8.2 Chignik rupture area (Ye et al., 2022; Figure 9c).

This deflection of the Contact Fault proxy around the Trinity Islands is spatially correlated with the western extent of the 4–5 m slip contours for the 1964 Great Alaska earthquake (Ichinose et al., 2007). It also coincides with a large 40–50 km wide high-velocity body imaged beneath the island that extends from the slab to within 2–3 km of

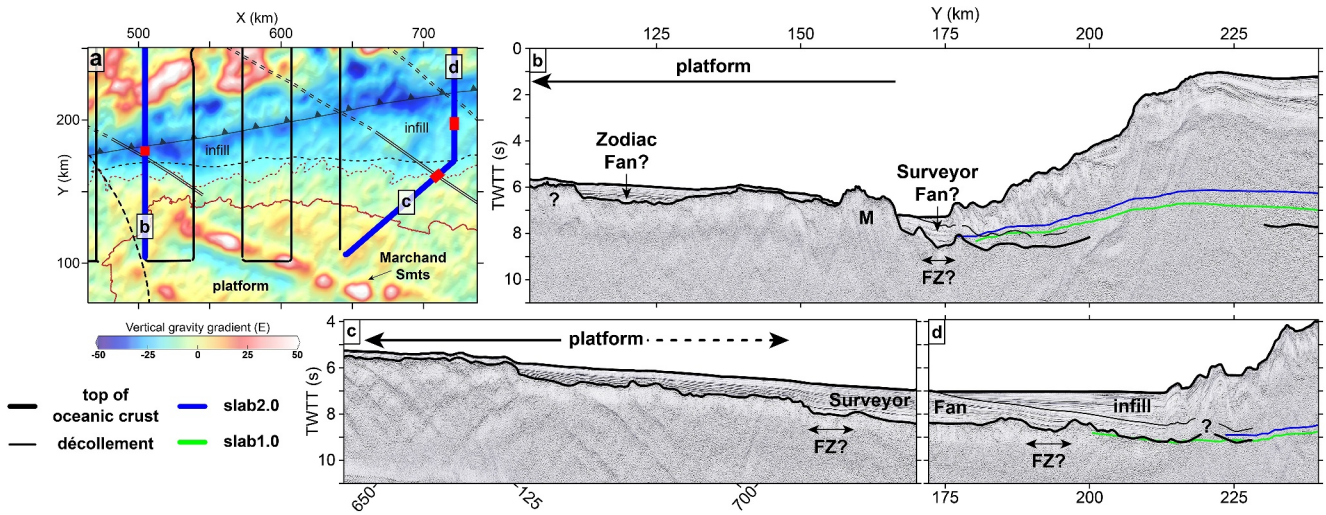

Figure 8. Post-stack time migrated sections from the MCS 4 km-long streamer data acquired during MGL1903 showing the northern flank of the platform outboard Kodiak and the eastern Semidi segment. (a) Blow up of the vertical gravity gradient map shown in Figure 1b, with blue lines corresponding to the stacks in (b)–(d) and red bars showing fracture zone locations interpreted on the stacked sections. Red line is the 4.5 km bathymetric contour, red dashed line marks the trenchward platform extent, and black dashed line indicates the onset of trench infill. (b–d) Stacks with time-converted velocities from the preferred model overlain. Double arrows show possible fracture zones locations from Choe and Dyment (2021).

the surface (Figures 4g, 5b, 6a, 6b, and 9a) and locally reduced slab velocities (<6 km/s) within a ~50 km-wide zone centered around the inferred downdip location of the Aja fracture zone (Choe & Dyment, 2021). The 6 m slip contour of the 1964 earthquake appears correlated with the fault proxy to the north and west. Additionally, large amounts of slip in 1964 (>6 m) correlate well with a broad increase in slab velocities, widening of the outer wedge, and trenchward extension of the crustal backstop. The 10 m slip contour (which approaches the trench) mirrors the 6.5 km/s slab velocity contour from the southeastern edge of Kodiak Island to more than 100 km updip (purple dashed lines in Figures 5b, 5c, and 9b).

5. Discussion

Our 3D P-wave velocity model across the Alaska Peninsula subduction zone sheds light on the long-wavelength velocity structure of both the incoming and overriding plates in the Semidi segment and SW Kodiak asperity regions. Here, we interpret our results together with bathymetry, gravity, magnetic, and MCS data. We then compare our results with previous studies and discuss potential controls on the observed variations in interseismic coupling and megathrust slip behavior within the SW Kodiak asperity, western, and eastern Semidi segments.

5.1. Structure and Properties of the Incoming Plate

5.1.1. The Effects of Late-Stage Magmatism

The incoming Pacific plate outboard of the Semidi segment encompasses two seamount chains (Figure 1, Figure S1 in Supporting Information S1): the Patton-Murray-Marchand seamount and Parker-Gilbert seamount groups along with their respective platforms (Wessel & Kroenke, 1998). In addition, in the western part of our study area, a small ridge structure (Bécel et al., 2015) is now clearly imaged with the AACSE bathymetry data (e.g., Figure 5a). We propose that a zone of weakness could have formed here during the plate reorganization at ~56 Ma that later facilitated intraplate magmatism from a shallow mantle source.

Crustal velocities directly beneath the Marchand Seamount group and in the platform just north of the seamounts appear normal to slightly reduced compared to the incoming plate average and the global Pacific crustal averages (Figure 7e, light and dark blue curves) (Grevemeyer et al., 2018) and within the range of recently reported values beneath other Pacific seamounts (Watts et al., 2021). Slightly lower velocities within 6 km directly beneath the Marchand lineament would suggest that the oceanic crust beneath the seamounts has a greater thickness of extrusive material compared to normal oceanic crust. In the lower crust and uppermost mantle, velocities are less than 8 km/s down to 17–18 km below the seafloor (Figure 7e). Without inverting for secondary arrivals to

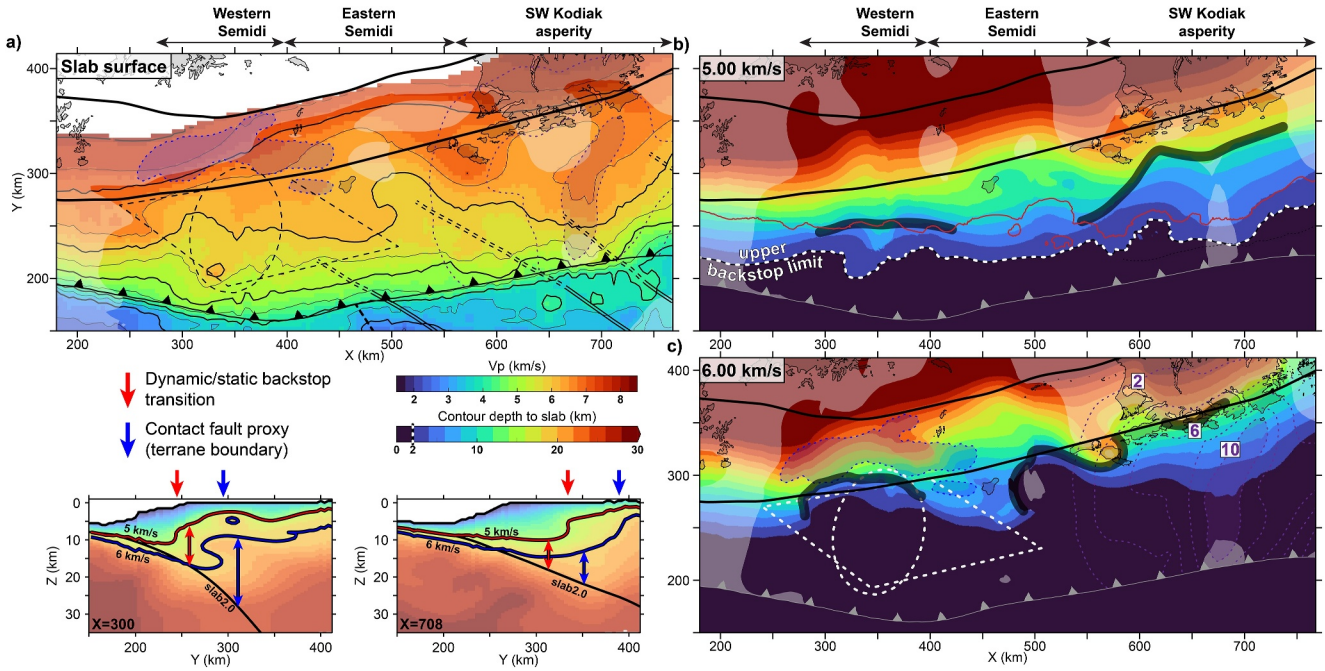

Figure 9. Velocity structure of the overriding plate and plate interface. (a) Velocities extracted along the Slab2.0 surface (Hayes et al., 2018). (b and c) Maps of thickness between the slab and 5 and 6 km/s iso-velocity contours, respectively. Red line is the 500 m bathymetric contour, blue dashed lines are the slab2.0 intersections from (a), dashed black/white lines are 2 km thickness, and thick transparent black lines are interpretations of strong gradient transitions (i.e., a backstop transition) in (b), and a terrane boundary in (c). Inset in the lower left-hand corner explains the thickness calculation and gradient interpretation (small arrows). CF: Contact Fault. White contours on the incoming plate are sediment thicknesses from Figure 7b (Clarke et al., 2024). All other markings are the same as in Figure 1b.

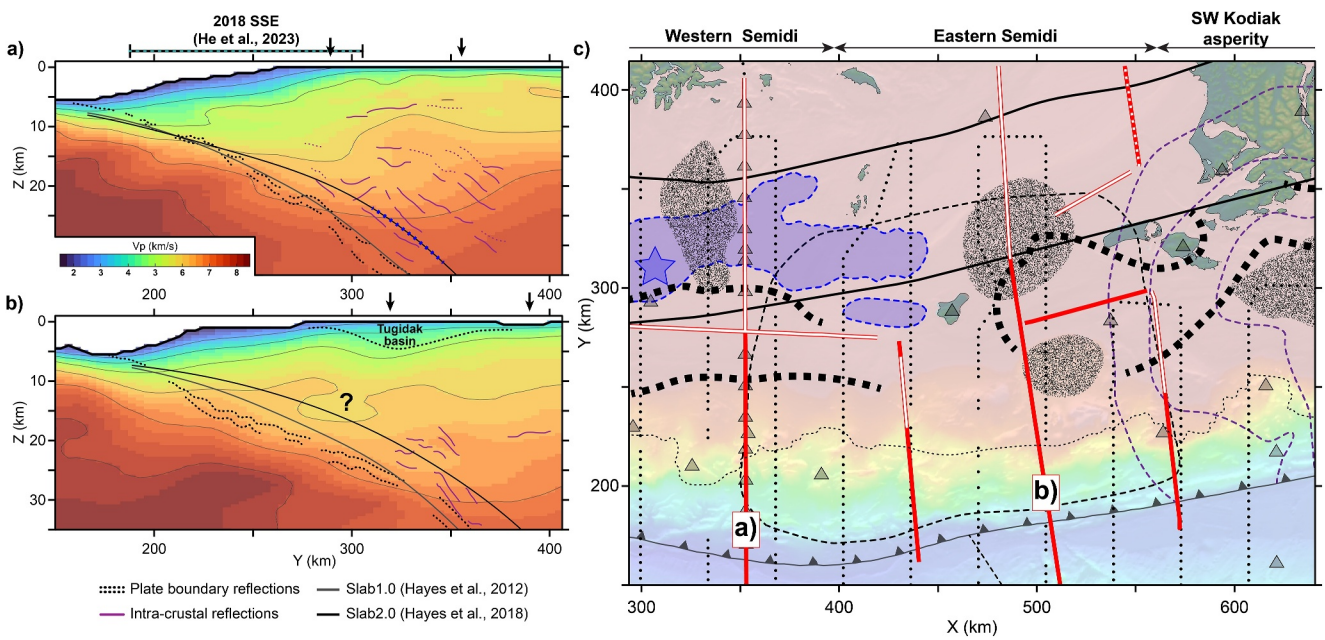

Figure 10. Model comparison with depth-migrated MCS images from the 2011 ALEUT survey (Kuehn, 2019). (a) Velocity slice taken along ALEUT line 3, with interpretations of the plate boundary and downgoing Pacific plate Moho (dotted black lines), intracrustal reflections (purple lines), and the slab1.0 and slab2.0 surfaces (black and gray solid lines, respectively; Hayes et al., 2012, 2018). Black arrows show the locations of the Contact Fault and Border and Ranges fault (Horowitz et al., 1989). Panel (b) same as in (a), but for ALEUT line 2-2R. (c) Bathymetric map of the study area showing profile locations in red. White lines show where intracrustal reflections are observed in the MCS images. Shaded areas are sedimentary basins from Figure 6a, and black dashed lines are the transitions identified in Figures 9a and 9b. Other markings are the same as those shown in Figure 1b.

constrain the Moho depth, it is difficult to determine whether velocity variations at greater depths beneath the lineament represent a sampling of a deflected oceanic crust below the seamounts (e.g., Grevemeyer et al., 2001; Watts et al., 2021), underplated magmatic or metasomatic material (Park & Rye, 2019; Richards et al., 2013), or both. We observe elevated lower-crustal (>7.5 km/s) and upper-mantle (>8 km/s) velocities on the southern edge of the Marchand seamounts and west of the ridge structure (Figures 7c and 7d); however, a lack of reversed ray coverage there could bias these results (Figure 3c). If nevertheless real, these elevated velocities could reflect crustal thickness variations and/or local depth variations in upper mantle anisotropy toward the southern edge of the platform (Grevemeyer et al., 2001).

5.1.2. The Contribution of Fracture Zones, Bend-Faulting, and Seamounts to Plate Hydration and Structure

Passive source S-wave seismic tomography (Li et al., 2024) shows that the upper mantle outboard of the SW Kodiak asperity, and to a lesser degree the upper oceanic mantle outboard of the Semidi segment, may be more hydrated than implied by previous Vp models derived from active source data (Krabbenhoeft et al., 2021; Shillington et al., 2015). Vp in areas where we see reduced values in our model are on average slightly below typical values expected for Pacific crust (Grevemeyer et al., 2018). Generally, our results are consistent with passive source S-wave models that indicate more pervasive and deeper hydration outboard Kodiak (Figure 6d) compared to the lower degree of hydration seen outboard of the Semidi segment (Figure 7); however, the different sources of crustal and mantle hydration remain poorly understood in the regions outboard of the Kodiak and Semidi segments.

Bending faults in the outer rise are commonly suggested to facilitate the incorporation of water into the subducting oceanic crust and upper mantle (Acquisto et al., 2022; Shillington et al., 2015). While significant bending faulting has been imaged west of the triple junction outboard the westernmost Semidi segment (Clarke et al., 2024), terminating at the ridge, few bending faults have been imaged in our study area (e.g., Figures 5a and 8). Fracture zones might also contain a more hydrated crust and upper mantle (Roland et al., 2012) that will deliver water to the subduction zone systems once subducted (Cooper et al., 2020; Paulatto et al., 2017). The higher degree of crustal and mantle hydration outboard Kodiak broadly corresponds with the presence of multiple E-W striking fracture zones (e.g., Choe & Dyment, 2021; Naugler & Wageman, 1973). Some of these fracture zones were possibly reactivated during the complex intraplate rupture along with pre-existing fabric that produced a Mw 7.9 earthquake in 2018 (Krabbenhoeft et al., 2018) (Figure 7, Figure S1b in Supporting Information S1). Many of these fracture zones are likely subducting (Ramos et al., 2022; von Huene et al., 2012) (Figure S2b in Supporting Information S1), possibly increasing the availability of water in the crust and uppermost mantle downdip. Because these fractures are small (~10 km wide) (Bécel et al., 2019; Figures 8b and 8c), we do not expect to resolve their structures individually, meaning any sampling of reduced Vp from pore and mineral-bound water will be averaged laterally there. Furthermore, the FZ seismic structure may reflect inherited complexity arising from possible multiple stages of magmatism at the paleo-ridge-transform intersection (e.g., Grevemeyer et al., 2021). Moreover, the precipitation of hydrous alteration products can seal cracks within old fracture zones, increasing Vp back toward normal values, as is inferred in the Aja fracture zone 1,100 km east of our study area (Christeson et al., 2022). It is important to note that P-waves are less sensitive to the presence of fluids and alteration products than S-waves or Vp/Vs and that upper mantle anisotropy might also contribute to the lack of a more significant Vp reduction in our model, as many raypaths outboard Kodiak are approximately parallel to the plate fabric (i.e., in the slow polarization direction) (Figure 3c).

Very subtle faulting seaward of Kodiak Island (around $X = 700–720$ km and $Y = 75–125$ km) has been interpreted as reactivated abyssal hill faults by plate bending (Reece et al., 2013); however, their structure and orientation are parallel to the plate fabric, which subducts obliquely to the trench and the principal direction of extensional stress, suggesting that other mechanisms might be at play (Figure 1b). From seismic imaging alone (Figure 8), it is difficult to rule out that some of these faults may have formed from differential compaction over a rougher basement. Alternatively, the outcrop of these faults on the platform could indicate that volcanic rejuvenation after the initial seamount formation (Keller et al., 1997) could have reactivated the abyssal hill fabric there and would contribute to observations of a hydrated incoming mantle (Li et al., 2024) and slab downdip (Gou et al., 2022; Wang et al., 2024). Indeed, metasomatic underplating during seamount formation can produce fractures leading to enhanced fluid circulation in the crust and upper mantle which, together with thermal buoyancy, might also explain the large extent of the platform (Park & Rye, 2019). This is further supported by geophysical evidence for

elevated pore and mineral-bound water in hydrothermally altered extrusive rocks subducting offshore New Zealand (e.g., Chesley et al., 2021; Gase et al., 2023) and observations of relatively high-water content and hydrothermal alteration products in dredged samples of the Murray Seamount (Dalrymple et al., 1987).

Therefore, while not nearly as altered as the Vp reductions in the crust and upper mantle suggest outboard the Shumagin Gap to the west (Acquisto et al., 2022; Shillington et al., 2015), the crust and mantle outboard the eastern Semidi segment and SW Kodiak asperity could be moderately hydrated due to the presence of fracture zones and hotspot metasomatic underplating. This is in agreement with recent Vs modeling (Li et al., 2024). These observations would be in accordance with the magnitude-frequency relationship of intermediate depth earthquakes (*b*-values) that implies a weakly, yet pervasively, hydrated crust and upper mantle there (Wei et al., 2021). Outboard the western Semidi segment ($X = 350$–500 km), our results favor even weaker (Li et al., 2024) and more local hydration of the incoming plate, most notably near the trench (Figures 7b and 7c) (Gou et al., 2022).

5.2. Relationship Between Incoming Plate Properties and Shallow Megathrust Properties

Several studies have proposed that the subduction of the Patton-Murray seamount chain could explain the semi-persistent segmentation between the SW Kodiak asperity and eastern Semidi segment (e.g., von Huene et al., 2012); however, the difference in orientation between the Marchand lineament and larger Patton-Murray seamounts complicates their downdip extrapolation (Figure 1 and Figure S1 in Supporting Information S1). Seamount and basement swell subduction might be corroborated just south of Chirikof Island by the presence of an upward bulge in the Slab2.0 surface between 10 and 15 km depth (Figures 6b and 6c) and locally elevated residual gravity anomalies in the outer wedge between $X = 450$ and 625 km (Figure S2a in Supporting Information S1). This coincides with our observations of more subdued vertical velocity gradients in the subducting oceanic crust between $X = 450$–550 km in our model (Figures 5c and 5d). While poor ray coverage and elevated standard deviation values (e.g., Figures S9e–S9g, S11a, and S11b in Supporting Information S1) around the slab bulge could indicate this feature is smeared vertically, other crustal-scale tomographic studies image low velocity roots of subducted seamounts as much as 40–50 km wide with reduced velocities extending 5–8 km below the adjacent Moho (e.g., Bassett et al., 2022; Kodaira et al., 2000; Paulatto et al., 2024; Warwel et al., 2024). Furthermore, a local reduction in mantle S-wave velocities in that area from recent 3D passive-source modeling could arise from a sampling of the subducting seamounts and platform in support of our interpretation (Li et al., 2024). Therefore, we propose that any larger seamounts and/or basement swell belonging to the Patton-Murray group and platform would have likely subducted just south and to the east of Chirikof Island (between $X = 450$–550 km) in the eastern Semidi segment, possibly contributing to the initial formation of the Trinity and Tugidak basins (Collot & Fisher, 1989) and a proposed transition in interseismic coupling there (Li & Freymueller, 2018; Wang et al., 2024; Xiao et al., 2021). Our interpretation is different than previous analysis from von Huene et al. (2015) that infer the short-wavelength residual gravity highs that extend NW of the pinch-out (Figure S2a in Supporting Information S1; between $X = 300$–425 km) to be an extension of the E-W trending Marchand lineament downdip that created the wide embayment there.

The large amounts of sediment entering the subduction zone within both the Semidi segment (Li et al., 2018) and SW Kodiak asperity (Krabbenhoeft et al., 2021) could contribute to relatively homogeneous plate interface, capable of generating large (Mw > 8) earthquakes such as the 2021 and 1964 earthquakes (Wang & Bilek, 2011, 2014); however, the possible role of variations in subducting sediment thickness and lithology remain unclear in this area. One of the clear contributions of the Patton-Murray seamount chain and platform has been to act as a barrier to the westward transport of Surveyor Fan sediments deposited outboard Kodiak Island (Reece et al., 2011; Stevenson et al., 1983; von Huene et al., 2012; Zhang & Gulick, 2019) (Figure 1). This is evidenced by a thinning of the bulk sediment cover atop the seamounts and platform (Figure 7b) and a pinching out of the trench fill around $X = 470$ km (Clarke et al., 2024). The AACSE bathymetry (Figure 4a), shallow velocity structure outboard the trench (Figure 5d), and MCS images (Figure 8) provide additional evidence for a link between the topography of the platform and changes in the incoming sediment thickness.

While thin sediment cover atop the platform supports previous interpretations that the Surveyor Fan does not extend far westward; it is likely that this fan is subducting in the eastern Semidi segment (Figures 8b and 8c). Zodiac Fan sediments are thickest outboard the western Semidi segment between $X = 280$–450 km (Figure 7b). Seismic images show a ~600 m thick layer of subducting Zodiac Fan turbidites inferred to be over-pressured at shallow depths (<10 km) (Li et al., 2018), and the geochemistry of arc magmas from the Alaska Peninsula show a

higher sediment contribution, suggesting the head of Zodiac Fan has subducted to great depths (von Huene et al., 2012; Wei et al., 2021). Higher pore-fluid pressures in the shallow megathrust could explain the slight decrease in plate coupling typically modeled from the eastern to western Semidi segments (Li & Freymueller, 2018), as well as low coupling near the trench as recently proposed (Wang et al., 2024; Xiao et al., 2021). At greater depths, consolidation of the thick, dewatered sediment channel could lead to increased coupling that leads to the nucleation of large earthquakes as previously proposed (Li et al., 2018; Shillington et al., 2015). We favor this interpretation given that coseismic slip during the 2021 Chignik event was confined to slab depths >25 km (Hayes et al., 2018; Ye et al., 2022) (Figure 1b) and is flanked updip by aseismic slow and postseismic slip (Brooks et al., 2023; He et al., 2023). High Vp/Vs ratios recovered in the downgoing plate within 50 km of the trench from local earthquake tomography also supports the presence of fluids and high fluid pore pressures (Gou et al., 2022; Wang et al., 2024) commonly invoked to explain shallow slow slip events (e.g., Saffer & Wallace, 2015).

East of the platform, subducting Surveyor Fan turbidites underlain by pelagic sediments smooth over a more moderately rough basement formed at intermediate spreading rates (Krabbenhoeft et al., 2021; Reece et al., 2013; von Huene et al., 2021). Unlike the 2021 Chignik event, the earthquake in 1938 appears to have nucleated at shallow depths and produced a small tsunami (Freymueller et al., 2021). Similarly, most slip on the SW Kodiak asperity in 1964 was confined to shallow depths (<20 km) beneath the Prince William terrane and extended near the trench (Ichinose et al., 2007) (Figure 1b). Our observation of elevated velocities along the slab surface seaward of Kodiak corresponds well with observations of increased shallow plate coupling and near-trench slip (Li & Freymueller, 2018) (Figure 9a). Furthermore, recent modeling of tsunami data from the 1938 Mw 8.3 earthquake (Freymueller et al., 2021) indicate that the shallow megathrust here might be capable of producing large shallow slip (Figure 1b). Evidence for vents near the trench located between the central SW Kodiak asperity and Chirikof Island (Figure 1b; Krabbenhoeft et al., 2021; von Huene et al., 2021) suggests that some dewatering is occurring at shallow depth although the efficiency of this process remains uncertain. These results contradict recent Vp/Vs constraints showing that the subducting slab and most of the megathrust may actually be fluid-rich in the eastern Semidi segment and SW Kodiak asperity (Wang et al., 2024). However, a lack of vertical resolution makes it unclear whether Vp/Vs ratio is high along the megathrust or within the subducting oceanic crust. Another important factor is the lithology of the subducting sediments that vary across the margin (Figures 7b and 8). Although it is likely that differences in the layering and lithology between the Surveyor and Zodiac Fans and other pelagic sequences (Creager et al., 1973; Reece et al., 2011) contribute to shallow segmentation observed within the Semidi segment (e.g., Namiki et al., 2014), the specific lithology differences cannot be directly inferred from our model and will require further focused studies. Therefore, we propose that contrasting amounts of free water available to the shallow megathrust coupled with the different sediment inputs may contribute to a greater propensity for shallow megathrust slip in the eastern Semidi segment and SW Kodiak asperity compared to that in the western Semidi segment.

5.3. Overriding Plate Architecture and Composition

5.3.1. Backstop Partitioning and Deformation in the Prince William Terrane

In the outer wedge, the position of our proxy for the updip limit of the backstop, or margin framework (where the 5 km/s iso-velocity contour reaches 2 km thickness with slab2.0), is in general agreement with the location of the mid-slope backstop splay fault zones seen in other studies for the Semidi segment (Li et al., 2018; von Huene et al., 2021) and SW Kodiak asperity (Krabbenhoeft et al., 2021) (Figure 9b). Elevated slab velocities in the eastern half of our model give rise to a shallower updip backstop limit that corresponds with coseismic slip and uplift near the trench in the eastern Semidi during the 1938 Mw 8.2-3 and in the SW Kodiak asperity during 1964 that was largely confined to the megathrust beneath the Prince William terrane (Freymueller et al., 2021; Ichinose et al., 2007; Suleimani & Freymueller, 2020) (Figure 1b). The gradual retreat of the backstop limit between $X = 400$–500 km broadly coincides with the aforementioned change in sediment inputs. Where the backstop is farthest from the trench just westward is also where slow and post-seismic slip likely occurred updip of the 2021 Chignik rupture area (Brooks et al., 2023; He et al., 2023). Given the limited resolution in our model around and along the shallow megathrust, any Vp variations related to sharp changes in lithology or consolidation state of the upper plate that might influence shallow frictional properties are likely smeared. However, our results and other evidence for contrasting slip behaviors both suggest a possible widening of the conditionally stable zone of the shallow megathrust in the western Semidi segment.

Further landward, we image a rapid decrease in the width of the dynamic backstop (Vp < 5 km/s) from >100 km outboard Kodiak Island, to <50 km in the Semidi segment that mirrors a change in outer slope morphology and the westward thinning of the Prince William terrane (Figure 9b). Our interpretation of this boundary corresponds well with location of the Ugak and other faults that reactivated in 1964 and in the past (Briggs et al., 2014), contributing to uplift and tsunamigenesis there (Suleimani & Freymueller, 2020), and which are also interpreted as evidence for downdip segmentation of the crustal backstop (Ramos et al., 2022) (Figures 1b and 8b). The lack of a clear jump in 5 km/s contours that we define as the backstop transition between $X = 425$–550 km (Figures 4f and 9b) may be in part due to a lack of ray coverage in the area; however, locally elevated velocities (>6 km/s) landward of the bulge in slab2.0 (Figures 6a and 6b) appear well-resolved (Figures S4 and S12b in Supporting Information S1) and could reflect over-consolidation of accreted rocks from the subduction of large Patton-Murray seamounts and platform (Sun et al., 2020). Alternatively, we could be imaging a seaward extension of higher-density plutonic rocks originating from the same magmatic event that formed the Kodiak batholith (Farris & Paterson, 2009; Horowitz et al., 1989). Both interpretations imply a thinning of the seismically defined dynamic backstop in the Semidi segment that reflects an along-margin material strength (i.e., rigidity) contrast in upper plate material within the Prince William terrane (Byrne et al., 1988; Kopp & Kukowski, 2003). Previous studies have shown the importance of overriding plate rigidity and backstop geometry on depth-varying rupture processes (Sallarès & Ranero, 2019; Watt & Brothers, 2020). In our study area, a frictional contrast along the seismogenic megathrust between the SW Kodiak asperity and eastern Semidi segment could be linked to along-strike variations in backstop strength and width. Therefore, we propose that in addition to possible subducting bathymetry like seamounts, a broad juxtaposition of contrasting overriding plate rheological properties provides further evidence for the semi-persistent rupture boundary there (Briggs et al., 2014).

5.3.2. Static Backstop and Chugach Terrane

Using the 6 km/s iso-velocity contour, we estimate the mid-crustal location of the Contact Fault that delineates the boundary between the Prince William and Chugach terranes (Figure 9c). In southcentral Alaska, this terrane boundary is associated with a similar jump in Vp to ~6 km/s (Fuis et al., 2008) that we recover across most of our model space (Figure 9c). In the SW Kodiak asperity, the 6 km/s proxy is centered around where the Contact Fault outcrops on Kodiak Island and approximately follows the speculated offshore extent inferred from gravity and magnetic data to the west (Horowitz et al., 1989). Most of the Chugach and parts of the Prince-William terranes are speculated to contain granitic and gabbroic plutons as well as some young accreted ophiolites that were emplaced in the early Paleocene as a segmented ridge subducted (Farris & Paterson, 2009; Horowitz et al., 1989). Overriding plate velocities beneath Kodiak Island are very high (>6.5 km/s) and mirror a long fault-parallel lineament seen the gravity data (Figure 1b, Figure S2a in Supporting Information S1) and outcrops of the Kodiak batholith (Bradley et al., 2003). Just southwest, we see similar evidence for large shallow high-velocity bodies (e.g., Figure 4b) with wavespeeds reaching 6.5 km/s within 5 km of the seafloor (Figure 6a). Neither the Contact Fault nor plutonic rocks outcrop on the adjacent Trinity Islands, which are composed of uplifted accreted rocks (e.g., Clendenen et al., 1992). Thus, while we cannot rule out a local seaward extension of the Chugach terrane, it is likely that this high-velocity body represents the subsurface extension of magmatism from a slab window (Farris, 2010) into the Prince William terrane (Horowitz et al., 1989; Moore et al., 1983).

Trench-parallel slices landward of the Contact Fault show that the extent of mid-crustal intrusions in the Chugach terrane may be reduced in the eastern Semidi segment (between $X = 400$–500 km; e.g., Figure 5b) where others have speculated sediment underplating beneath a wide gravity low there (Figure 1, Figure S1 in Supporting Information S1) (Ramos et al., 2022). While we cannot confirm the presence of underplated sediments, overriding plate velocities are slightly reduced at all depths where the intracrustal reflections in the Chugach terrane imaged along AL02 appear restricted to greater depths (>18–20 km), closer to the slab surface (Figure 10) (Kuehn, 2019). Both a lesser degree of intrusions and/or underplated sediments could serve to locally decrease upper plate velocities, and thus rigidity there. To the west (between $X = 350$–400 km), multiple lines of evidence, including increased Vp (Figure 6), a magnetic high (Figure S1b in Supporting Information S1), abundant intracrustal reflections from the plate interface to <10 km depth (Figure 10), and low Vp/Vs ratios (Wang et al., 2024) above the slab indicate the presence of more extensive intrusions within the area of slip modeled for the 2021 Chignik event (Figures 6 and 10) (Ye et al., 2022). Terranes consisting largely of high-density intrusive material increase the overburden, possibly contributing to enhanced sediment consolidation, increased fault strength, and high plate coupling within the Chugach terrane of the western Semidi segment. Indeed, high-density material has been

implicated in localizing large amounts of slip during great earthquakes (e.g., Bassett et al., 2016) and have also been imaged in the Chugach terrane to the west, within the Shumagin gap, where other large earthquakes have nucleated (Shillington et al., 2022). Furthermore, if the relative decrease in Vp to the east represents a decrease in rigidity of the upper plate, this might contribute to the gravity low there and explain why the 2021 Chignik event did not rupture into the eastern Semidi segment.

6. Conclusions

We use 3D active-source OBS data to produce a crustal-scale Vp model of the Alaska Peninsula subduction zone that encompasses the incoming and overriding plates within the SW Kodiak asperity and Semidi segment. On the incoming plate, we observe modest velocity variations that we attribute to the effects of late-stage magmatism that formed the Patton-Murray and Marchand seamounts and basement swell and the presence of a series of fracture zones. Based on our observed velocity variations across the incoming plate, we propose that fracture zones and hotspot magmatism significantly contribute to the hydration of the crust and possibly the uppermost mantle. Our velocity model together with the AACSE MCS images detail the extent of these bathymetric features and show how they modulate the thickness and type of sediments entering the system. We propose that these variations contribute to the observed variations in rupture pattern and coupling.

In the overriding plate, our model reveals large-scale along-margin changes in the updip limit of the backstop, or margin framework, and width of a proposed actively deforming dynamic backstop within the Prince William terrane. In the SW Kodiak asperity and eastern Semidi segment, the shallow limit of the seismogenic zone likely extends to within 40–50 km from the trench where splay faults have been imaged, and large amounts shallow slip occurred in 1938 and 1964. Evidence for a wider dynamic backstop seaward of Kodiak Island corresponds with past observations of uplift and deformation that contributed to the local tsunami in 1964. Just downdip, we show that the subsurface extent of the Kodiak batholith is likely greater than can inferred from outcrops on Kodiak Island and could have contributed to localization of slip in 1964.

While the shallow megathrust in eastern Semidi is capable of producing rapid slip during large earthquakes, a possible combination of subducting Patton-Murray seamounts and platform, fracture zones, and/or extensive intrusions in the Prince William terrane could produce frictional heterogeneities that explain why this area seems to act as a semi-persistent barrier to rupture propagation.

In the western Semidi segment, we interpret a landward retreat of the seismogenic zone (i.e., a widening of the frictionally stable regime) where subducting, overpressured Zodiac Fan sediments decrease shallow plate coupling and facilitate slow slip. Landward of the slope break, within the Chugach terrane, we see evidence widespread for intrusions around where slip was localized during the 2021 Chignik earthquake. An overall decrease in rigidity beneath a gravity low to the east could create a frictional contrast that explains why rupture during 2021 did not extend farther east.

In summary, our results point toward a more nuanced view of segmentation between the SW Kodiak asperity and the eastern Semidi segment that arises from a confluence of subducting topography on the incoming plate, variable backstop architecture, and compositional (rigidity) changes within the Chugach and Prince William terranes. Our results agree with recent evidence that megathrust may be further segmented between the eastern and western Semidi segments, which could in part be explained by the subduction of different sedimentary fans, additional subducting topography, and shallow hydrological processes.

Data Availability Statement

The 3D P-wave velocity model obtained from this study and corresponding navigation files are available in Acquisto et al. (2024). OBS SEGY data from the AACSE Airgun shooting supplement are available in Abers et al. (2018). OBS SEGY data from ALEUT Line 3 are available in Shillington (2011). Continuous data from onshore station S19K, SII, CHI, CHN are available from the EarthScope/IRIS DMC. Raw marine seismic reflection data are available in Bécel et al. (2019). Relocated earthquake locations were downloaded from the USGS web service by selecting the "aacse" catalog. The tomographic code used in this study is available in Meléndez et al. (2015). Earthquake locations were obtained using NonLinLoc (Lomax et al., 2000), PyKonal (White et al., 2020), and BPMF (Beaucé et al., 2024).

Acknowledgments
We gratefully acknowledge the AACSE PIs, early career scientist volunteers, OBS technicians from LDEO and WHOI, captains, and crews of R/V *Sikuliaq* cruises SKQ201811S and SKQ201816S and R/V *Marcus G. Langseth* cruises MGL1110 and MGL1903 for their efforts in deploying and recovering the ocean bottom seismometers and acquiring the active-source data sets used in this study. We thank Shearwater for providing academic licenses for the seismic processing software used in this study. We are also grateful to Andrew Gase and an anonymous reviewer who provided insightful comments and suggestions which greatly improved this paper. This research was supported by the NSF Grant OCE-1947758 to Lamont and OCE-1948087 to WHOI.

References

Abers, G., Wiens, D., Schwartz, S., Sheehan, A., Shillington, S., Worthington, L., et al. (2018). AACSE: Alaska amphibious community seismic experiment [Dataset]. *International Federation of Digital Seismograph Networks*. https://doi.org/10.7914/SN/XO_2018

Acquisto, T., Bécel, A., Canales, J., & Beaucé, E. (2024). 3D P-wave velocity model of the Alaska Peninsula subduction zone from the AACSE active-source data set [Dataset]. *MGDS*. https://doi.org/10.60521/331829

Acquisto, T., Bécel, A., Singh, S. C., & Carton, H. (2022). Evidence of strong upper oceanic crustal hydration outboard the Alaskan and Sumatran subduction zones. *Journal of Geophysical Research: Solid Earth*, *127*(10), e2022JB024751. https://doi.org/10.1029/2022JB024751

Arnulf, A. F., Bassett, D., Harding, A. J., Kodaira, S., Nakanishi, A., & Moore, G. (2022). Upper-plate controls on subduction zone geometry, hydration and earthquake behaviour. *Nature Geoscience*, *15*(2), 143–148. https://doi.org/10.1038/s41561-021-00879-x

Bangs, N. L., McIntosh, K. D., Silver, E. A., Kluesner, J. W., & Ranero, C. R. (2015). Fluid accumulation along the Costa Rica subduction thrust and development of the seismogenic zone. *Journal of Geophysical Research: Solid Earth*, *120*(1), 67–86. https://doi.org/10.1002/2014JB011265

Barcheck, G., Abers, G. A., Adams, A. N., Bécel, A., Collins, J., Gaherty, J. B., et al. (2020). The Alaska amphibious community seismic experiment. *Seismological Research Letters*, *91*(6), 3054–3063. https://doi.org/10.1785/0220200189

Bassett, D., Arnulf, A., Kodaira, S., Nakanishi, A., Harding, A., & Moore, G. (2022). Crustal structure of the Nankai subduction zone revealed by two decades of onshore-offshore and ocean-bottom seismic data: Implications for the dimensions and slip behavior of the seismogenic zone. *Journal of Geophysical Research: Solid Earth*, *127*(10), e2022JB024992. https://doi.org/10.1029/2022JB024992

Bassett, D., Sandwell, D. T., Fialko, Y., & Watts, A. B. (2016). Upper-plate controls on co-seismic slip in the 2011 magnitude 9.0 Tohoku-Oki earthquake. *Nature*, *531*(7592), 92–96. https://doi.org/10.1038/nature16945

Bassett, D., & Watts, A. B. (2015a). Gravity anomalies, crustal structure, and seismicity at subduction zones: 2. Interrelationships between fore-arc structure and seismogenic behavior. *Geochemistry, Geophysics, Geosystems*, *16*(5), 1541–1576. https://doi.org/10.1002/2014GC005685

Beaucé, E., Frank, W. B., Seydoux, L., Poli, P., Groebner, N., van der Hilst, R. D., & Campillo, M. (2024). BPMF: A backprojection and matched-filtering workflow for automated earthquake detection and location [Software]. *Seismological Research Letters*, *95*(2A), 1030–1042. https://doi.org/10.1785/0220230230

Bécel, A., Sheehan, A., Foster, D., Myers, E., Haeussler, P., Abers, G., et al. (2019). Multi-channel seismic shot data from the Alaska-Aleutians area acquired during Langseth cruise MGL1903 (2019) [Dataset]. *MGDS*. https://doi.org/10.1594/IEDA/324793

Bécel, A., Shillington, D. J., Nedimović, M. R., Webb, S. C., & Kuehn, H. (2015). Origin of dipping structures in fast-spreading oceanic lower crust offshore Alaska imaged by multichannel seismic data. *Earth and Planetary Science Letters*, *424*, 26–37. https://doi.org/10.1016/j.epsl.2015.05.016

Bilek, S. L. (2010). Invited review paper: Seismicity along the South American subduction zone: Review of large earthquakes, tsunamis, and subduction zone complexity. *Tectonophysics*, *495*(1), 2–14. https://doi.org/10.1016/j.tecto.2009.02.037

Bradley, D. C., Kusky, T. M., Haeussler, P. J., Goldfarb, R. J., Miller, M. L., Dumoulin, J. A., et al. (2003). Geologic signature of early tertiary ridge subduction in Alaska. *Geological Society of America Special Paper*, *371*, 19–49. https://doi.org/10.1130/0-8137-2371-X.19

Briggs, R. W., Engelhart, S. E., Nelson, A. R., Dura, T., Kemp, A. C., Haeussler, P. J., et al. (2014). Uplift ad subsidence reveal a nonpersistent megathrust rupture boundary (Sitkinak Island, Alaska). *Geophysical Research Letters*, *41*(7), 2289–2296. https://doi.org/10.1002/2014GL059380

Brocher, T. M. (2005). Empirical relations between elastic wavespeeds and density in the Earth's crust. *Bulletin of the Seismological Society of America*, *95*(6), 2081–2092. https://doi.org/10.1785/0120050077

Brooks, B. A., Goldberg, D., DeSanto, J., Ericksen, T. L., Webb, S. C., Nooner, S. L., et al. (2023). Rapid shallow megathrust afterslip from the 2021 M8.2 Chignik, Alaska earthquake revealed by seafloor geodesy. *Science Advances*, *9*(17), eadf9299. https://doi.org/10.1126/sciadv.adf9299

Bruns, T. R., Von Huene, R., Culotta, R. D., Lewis, S. D., & Ladd, J. W. (1987). Geology and petroleum potential of Shumagin continental margin, western Gulf of Alaska. In *Geology and resource potential of the Western North America and adjacent ocean basins-Beaufort Sea to Baja California* (Vol. 6, pp. 157–189).

Byrne, D. E., Davis, D. M., & Sykes, L. R. (1988). Loci and maximum size of thrust earthquakes and the mechanics of the shallow region of subduction zones. *Tectonics*, *7*(4), 833–857. https://doi.org/10.1029/TC007i004p00833

Canales, J. P., Carbotte, S. M., Nedimović, M. R., & Carton, H. (2017). Dry Juan de Fuca slab revealed by quantification of water entering Cascadia subduction zone. *Nature Geoscience*, *10*(11), 864–870. https://doi.org/10.1038/ngeo3050

Carlson, R. L., & Miller, D. J. (2003). Mantle wedge water contents estimated from seismic velocities in partially serpentinized peridotites. *Geophysical Research Letters*, *30*(5), 1250. https://doi.org/10.1029/2002GL016600

Chesley, C., Naif, S., Key, K., & Bassett, D. (2021). Fluid-rich subducting topography generates anomalous forearc porosity. *Nature*, *595*(7866), 255–260. https://doi.org/10.1038/s41586-021-03619-8

Chlieh, M., Perfettini, H., Tavera, H., Avouac, J. P., Remy, D., Nocquet, J. M., et al. (2011). Interseismic coupling and seismic potential along the central Andes subduction zone. *Journal of Geophysical Research*, *116*(B12), B12405. https://doi.org/10.1029/2010JB008166

Choe, H., & Dyment, J. (2021). The fate of marine magnetic anomaly in subduction zones: A global appraisal. *Earth and Planetary Science Letters*, *561*, 116787. https://doi.org/10.1016/j.epsl.2021.116787

Christeson, G. L., Goff, J. A., & Reece, R. S. (2019). Synthesis of oceanic crustal structure from two-dimensional seismic profiles. *Reviews of Geophysics*, *57*(2), 504–529. https://doi.org/10.1029/2019RG00064

Christeson, G. L., Gulick, S. P., Walton, M. A., & Barth, G. A. (2022). Seismic evidence for magmatic underplating along the Kodiak-Bowie seamount chain, Gulf of Alaska. *Tectonophysics*, *845*, 229639. https://doi.org/10.1016/j.tecto.2022.229639

Clarke, J., Shillington, D. J., Regalla, C., Gaherty, J. B., Estep, J., Wiens, D. A., et al. (2024). Controls on bending-related faulting offshore of the Alaska Peninsula. *Geochemistry, Geophysics, Geosystems*, *25*(3), e2023GC011271. https://doi.org/10.1029/2023GC011271

Clendenen, W. S., Sliter, W. V., & Byrne, T. (1992). Tectonic implications of the Albatross sedimentary sequence, Sitkinak Island, Alaska. In D. C. Bradley, & A. B. Ford (Eds.), *Geologic studies in Alaska by the U.S. Geological Survey, 1990* (Vol. 1999, pp. 52–70). U.S. Geological Survey Bulletin.

Collot, J. Y., & Fisher, M. A. (1989). Formation of forearc basins by collision between seamounts and accretionary wedges: An example from the New Hebrides subduction zone. *Geology*, *17*(10), 930–933. https://doi.org/10.1130/0091-7613(1989)017%3C0930:FOFBBC%3E2.3.CO;2

Collot, J. Y., Marcaillou, B., Sage, F., Michaud, F., Agudelo, W., Charvis, P., et al. (2004). Are rupture zone limits of great subduction earthquakes controlled by upper plate structures? Evidence from multichannel seismic reflection data acquired across the northern Ecuador–southwest Colombia margin. *Journal of Geophysical Research*, *109*(B11), B11103. https://doi.org/10.1029/2004JB003060

Cooper, G. F., Macpherson, C. G., Blundy, J. D., Maunder, B., Allen, R. W., Goes, S., et al. (2020). Variable water input controls evolution of the Lesser Antilles volcanic arc. *Nature*, *582*(7813), 525–529. https://doi.org/10.1038/s41586-020-2407-5

Creager, J. S., Scholl, D. W., Boyce, R. E., Echols, R. J., Fullam, T. J., Grow, J. A., et al. (1973). Site 183. *Initial Reports of the Deep Sea Drilling Project*, *19*. https://doi.org/10.2973/dsdp.proc.19.102.1973

Dalrymple, G. B., Clague, D. A., Vallier, T. L., & Menard, H. W. (1987). $^{40}Ar/^{39}Ar$ age, petrology, and tectonic significance of some seamounts in the Gulf of Alaska. In *Seamounts, islands, and atolls* (pp. 297–315). American Geophysical Union (AGU). https://doi.org/10.1029/GM043p0297

Davies, J., Sykes, L., House, L., & Jacob, K. (1981). Shumagin seismic gap, Alaska Peninsula: History of great earthquakes, tectonic setting, and evidence for high seismic potential. *Journal of Geophysical Research*, *86*(B5), 3821–3855. https://doi.org/10.1029/JB086iB05p03821

DeMets, C., Gordon, R. G., & Argus, D. F. (2010). Geologically current plate motions. *Geophysical Journal International*, *181*(1), 1–80. https://doi.org/10.1111/j.1365-246X.2009.04491.x

Desonie, D. L., & Duncan, R. A. (1990). The Cobb-Eickelberg seamount chain: Hotspot volcanism with mid-ocean ridge basalt affinity. *Journal of Geophysical Research*, *95*(B8), 12697–12711. https://doi.org/10.1029/JB095iB08p12697

Doser, D. I., Brown, W. A., & Velasquez, M. (2002). Seismicity of the Kodiak Island Region (1964-2001) and its relation to the 1964 Great Alaska earthquake. *Bulletin of the Seismological Society of America*, *92*(8), 3269–3292. https://doi.org/10.1785/0120010280

Drooff, C., & Freymueller, J. T. (2021). New constraints on slip deficit on the Aleutian megathrust and inflation at Mt. Veniaminof, Alaska from repeat GPS measurements. *Geophysical Research Letters*, *48*(4), e2020GL091787. https://doi.org/10.1029/2020GL091787

Elliott, J. L., Grapenthin, R., Parameswaran, R. M., Xiao, Z., Freymueller, J. T., & Fusso, L. (2022). Cascading rupture of a megathrust. *Science Advances*, *8*(18), eabm4131. https://doi.org/10.1126/sciadv.abm4131

Engebretson, D. C., Cox, A., & Gordon, R. G. (1984). Relative motions between oceanic plates of the pacific basin. *Journal of Geophysical Research*, *89*(B12), 10291–10310. https://doi.org/10.1029/JB089iB12p10291

Farris, D. W. (2010). Tectonic and petrologic evolution of the Kodiak batholith and the trenchward belt, Kodiak Island, AK: Contact fault juxtaposition? *Journal of Geophysical Research*, *115*(B7), B07208. https://doi.org/10.1029/2009JB006434

Farris, D. W., & Paterson, S. R. (2009). Subduction of a segmented ridge along a curved continental margin: Variations between the western and eastern Sanak–Baranof belt, southern Alaska. *Tectonophysics*, *464*(1), 100–117. https://doi.org/10.1016/j.tecto.2007.10.008

Fisher, M. A. (1979). Structure and tectonic setting of continental shelf southwest of Kodlak Island, Alaska. *AAPG Bulletin*, *63*(3), 301–310. https://doi.org/10.1306/C1EA55FD-16C9-11D7-8645000102C1865D

Flores, P. C. M., Kodaira, S., Kimura, G., Shiraishi, K., Nakamura, Y., Fujie, G., et al. (2024). Link between geometrical and physical property changes along Nankai Trough with slow earthquake activity revealed by dense reflection survey. *Geophysical Research Letters*, *51*(8), e2023GL106662. https://doi.org/10.1029/2023GL106662

French, M. E., & Condit, C. B. (2019). Slip partitioning along an idealized subduction plate boundary at deep slow slip conditions. *Earth and Planetary Science Letters*, *528*, 115828. https://doi.org/10.1016/j.epsl.2019.115828

Freymueller, J. T., Suleimani, E. N., & Nicolsky, D. J. (2021). Constraints on the slip distribution of the 1938 Mw 8.3 Alaska Peninsula earthquake from tsunami modeling. *Geophysical Research Letters*, *48*(9), e2021GL092812. https://doi.org/10.1029/2021GL092812

Fuis, G. S., Moore, T. E., Plafker, G., Brocher, T. M., Fisher, M. A., Mooney, W. D., et al. (2008). Trans-Alaska Crustal Transect and continental evolution involving subduction underplating and synchronous foreland thrusting. *Geology*, *36*(3), 267–270. https://doi.org/10.1130/G24257A.1

Fujii, Y., Satake, K., Sakai, S., Shinohara, M., & Kanazawa, T. (2011). Tsunami source of the 2011 off the pacific coast of Tohoku earthquake. *Earth Planets and Space*, *63*(7), 815–820. https://doi.org/10.5047/eps.2011.06.010

Gase, A. C., Bangs, N. L., Saffer, D. M., Han, S., Miller, P. K., Bell, R. E., et al. (2023). Subducting volcaniclastic-rich upper crust supplies fluids for shallow megathrust and slow slip. *Science Advances*, *9*(33), eadh0150. https://doi.org/10.1126/sciadv.adh0150

Gou, T., Xia, S., Huang, Z., & Zhao, D. (2022). Structural heterogeneity of the Alaska-Aleutian forearc: Implications for interplate coupling and seismogenic behaviors. *Journal of Geophysical Research: Solid Earth*, *127*(11), e2022JB024621. https://doi.org/10.1029/2022JB024621

Grevemeyer, I., Flueh, E. R., Reichert, C., Bialas, J., Kläschen, D., & Kopp, C. (2001). Crustal architecture and deep structure of the Ninety East Ridge hotspot trail from active-source ocean bottom seismology. *Geophysical Journal International*, *144*(2), 414–431. https://doi.org/10.1046/j.0956-540X.2000.01334.x

Grevemeyer, I., Ranero, C. R., & Ivandic, M. (2018). Structure of oceanic crust and serpentinization at subduction trenches. *Geosphere*, *14*(2), 395–418. https://doi.org/10.1130/GES01537.1

Grevemeyer, I., Rüpke, L. H., Morgan, J. P., Iyer, K., & Devey, C. W. (2021). Extensional tectonics and two-stage crustal accretion at oceanic transform faults. *Nature*, *591*(7850), 402–407. https://doi.org/10.1038/s41586-021-03278-9

Haeussler, P. J., Armstrong, P. A., Liberty, L. M., Ferguson, K. M., Finn, S. P., Arkle, J. C., & Pratt, T. L. (2015). Focused exhumation along megathrust splay faults in Prince William Sound, Alaska. *Quaternary Science Reviews*, *113*, 8–22. https://doi.org/10.1016/j.quascirev.2014.10.013

Hayes, G. P., Moore, G. L., Portner, D. E., Hearne, M., Flamme, H., Furtney, M., & Smoczyk, G. M. (2018). Slab2, a comprehensive subduction zone geometry model. *Science*, *362*(6410), 58–61. https://doi.org/10.1126/science.aat4723

Hayes, G. P., Wald, D. J., & Johnson, R. L. (2012). Slab1.0: A three-dimensional model of global subduction zone geometries. *Journal of Geophysical Research*, *117*(B1), B01302. https://doi.org/10.1029/2011JB008524

He, B., Wei, X., Wei, M., Shen, Y., Alvarez, M., & Schwartz, S. Y. (2023). A shallow slow slip event in 2018 in the Semidi segment of the Alaska subduction zone detected by machine learning. *Earth and Planetary Science Letters*, *612*, 118154. https://doi.org/10.1016/j.epsl.2023.118154

Horowitz, W. L., Steffy, D. A., Hoose, P. J., & Turner, R. F. (1989). *Geologic report for the Shumagin planning area, western Gulf of Alaska. Final report. OCS Report, MMS 89-0097*. U.S. Department of the Interior, Minerals Management Service, Alaska OCS Region.

Hyndman, R. D., Yamano, M., & Oleskevich, D. A. (1997). The seismogenic zone of subduction thrust faults. *Island Arc*, *6*(3), 244–260. https://doi.org/10.1111/j.1440-1738.1997.tb00175.x

Ichinose, G., Somerville, P., Thio, H. K., Graves, R., & O'Connell, D. (2007). Rupture process of the 1964 Prince William Sound, Alaska, earthquake from the combined inversion of seismic, tsunami, and geodetic data. *Journal of Geophysical Research*, *112*(B7), B07306. https://doi.org/10.1029/2006JB004728

Ito, Y., Tsuji, T., Osada, Y., Kido, M., Inazu, D., Hayashi, Y., et al. (2011). Frontal wedge deformation near the source region of the 2011 Tohoku-Oki earthquake. *Geophysical Research Letters*, *38*(7), L00G05. https://doi.org/10.1029/2011GL048355

Johnson, J. M., Satake, K., Holdahl, S. R., & Sauber, J. (1996). The 1964 Prince William Sound earthquake: Joint inversion of tsunami and geodetic data. *Journal of Geophysical Research*, *101*(B1), 523–532. https://doi.org/10.1029/95JB02806

Keller, R. A., Fisk, M. R., Duncan, R. A., & White, W. M. (1997). 16 m.y. of hotspot and nonhotspot volcanism on the Patton-Murray seamount platform, Gulf of Alaska. *Geology*, *25*(6), 511–514. https://doi.org/10.1130/0091-7613(1997)025%3C0511:MYOHAN%3E2.3.CO;2

Kodaira, S., Takahashi, N., Nakanishi, A., Miura, S., & Kaneda, Y. (2000). Subducted seamount imaged in the rupture zone of the 1946 Nankaido earthquake. *Science*, *289*(5476), 104–106. https://doi.org/10.1126/science.289.5476.104

Kopp, H., & Kukowski, N. (2003). Backstop geometry and accretionary mechanics of the Sunda margin. *Tectonics*, *22*(6). https://doi.org/10.1029/2002TC001420

Korenaga, J., Holbrook, W. S., Kent, G. M., Kelemen, P. B., Detrick, R. S., Larsen, H. C., et al. (2000). Crustal structure of the southeast Greenland margin from joint refraction and reflection seismic tomography. *Journal of Geophysical Research*, *105*(B9), 21591–21614. https://doi.org/10.1029/2000JB900188

Krabbenhoeft, A., von Huene, R., Miller, J. J., & Klaeschen, D. (2021). Subducting oceanic basement roughness impacts on upper-plate tectonic structure and a backstop splay fault zone activated in the southern Kodiak aftershock region of the Mw 9.2, 1964 megathrust rupture, Alaska. *Geosphere*, *17*(2), 409–437. https://doi.org/10.1130/GES02275.1

Krabbenhoeft, A., von Huene, R., Miller, J. J., Lange, D., & Vera, F. (2018). Strike-slip 23 January 2018 Mw 7.9 Gulf of Alaska rare intraplate earthquake: Complex rupture of a fracture zone system. *Scientific Reports*, *8*(1), 13706. https://doi.org/10.1038/s41598-018-32071-4

Kuehn, H. (2019). *Along-trench segmentation and down-dip limit of the seismogenic zone at the eastern Alaska-Aleutian subduction zone (PhD thesis)*. Dalhousie University. Retrieved from https://dalspace.library.dal.ca/handle/10222/75145

Lay, T., Kanamori, H., Ammon, C. J., Koper, K. D., Hutko, A. R., Ye, L., et al. (2012). Depth-varying rupture properties of subduction zone megathrust faults. *Journal of Geophysical Research*, *117*(B4), B04311. https://doi.org/10.1029/2011JB009133

Li, J., Shillington, D. J., Saffer, D. M., Bécel, A., Nedimović, M. R., Kuehn, H., et al. (2018). Connections between subducted sediment, pore-fluid pressure, and earthquake behavior along the Alaska megathrust. *Geology*, *46*(4), 299–302. https://doi.org/10.1130/G39557.1

Li, S., & Freymueller, J. T. (2018). Spatial variation of slip behavior beneath the Alaska Peninsula along Alaska-Aleutian subduction zone. *Geophysical Research Letters*, *45*(8), 3453–3460. https://doi.org/10.1002/2017GL076761

Li, Z., Wiens, D. A., Shen, W., & Shillington, D. J. (2024). Along-strike variations of Alaska subduction zone structure and hydration determined from amphibious seismic data. *Journal of Geophysical Research: Solid Earth*, *129*(3), e2023JB027800. https://doi.org/10.1029/2023JB027800

Liu, C., Bai, Y., Lay, T., Feng, Y., & Xiong, X. (2023). Megathrust complexity and the up-dip extent of slip during the 2021 Chignik, Alaska Peninsula earthquake. *Tectonophysics*, *854*, 229808. https://doi.org/10.1016/j.tecto.2023.229808

Lomax, A., Virieux, J., Volant, P., & Berge-Thierry, C. (2000). Probabilistic earthquake location in 3D and layered models [Software]. In *Advances in seismic event location* (pp. 101–134). Springer. https://doi.org/10.1007/978-94-015-9536-0_5

Malinverno, A., Quigley, K. W., Staro, A., & Dyment, J. (2020). A late Cretaceous-Eocene geomagnetic polarity timescale (MQSD20) that steadies spreading rates on multiple mid-ocean ridge flanks. *Journal of Geophysical Research: Solid Earth*, *125*(8), e2020JB020034. https://doi.org/10.1029/2020JB020034

Mankhemthong, N., Doser, D. I., & Pavlis, T. L. (2013). Interpretation of gravity and magnetic data and development of two-dimensional cross-sectional models for the Border Ranges fault system, south-central Alaska. *Geosphere*, *9*(2), 242–259. https://doi.org/10.1130/GES00833.1

Meléndez, A., Korenaga, J., Sallarès, V., Miniussi, A., & Ranero, C. (2015). TOMO3D: 3-D joint refraction and reflection traveltime tomography parallel code for active-source seismic data—Synthetic test [Software]. *Geophysical Journal International*, *203*(1), 158–174. https://doi.org/10.1093/gji/ggv292

Moore, J. C., Byrne, T., Plumley, P. W., Reid, M., Gibbons, H., & Coe, R. S. (1983). Paleogene evolution of the Kodiak islands, Alaska: Consequences of ridge-trench interaction in a more southerly latitude. *Tectonics*, *2*(3), 265–293. https://doi.org/10.1029/TC002i003p00265

Moser, T. J. (1991). Shortest path calculation of seismic rays. *Geophysics*, *56*(1), 59–67. https://doi.org/10.1190/1.1442958

Moser, T. J., Nolet, G., & Snieder, R. (1992). Ray bending revisited. *Bulletin of the Seismological Society of America*, *82*(1), 259–288. https://doi.org/10.1785/BSSA0820010259

Namiki, Y., Tsutsumi, A., Ujiie, K., & Kameda, J. (2014). Frictional properties of sediments entering the Costa Rica subduction zone offshore the Osa Peninsula: Implications for fault slip in shallow subduction zones. *Earth Planets and Space*, *66*(1), 72. https://doi.org/10.1186/1880-5981-66-72

Naugler, F. P., & Wageman, J. M. (1973). Gulf of Alaska: Magnetic anomalies, fracture zones, and plate interaction. *Geological Society of America Bulletin*, *84*(5), 1575–1584. https://doi.org/10.1130/0016-7606(1973)84⟨1575:GOAMAF⟩2.0.CO;2

Nishikawa, T., Matsuzawa, T., Ohta, K., Uchida, N., Nishimura, T., & Ide, S. (2019). The slow earthquake spectrum in the Japan Trench illuminated by the S-Net seafloor observatories. *Science*, *365*(6455), 808–813. https://doi.org/10.1126/science.aax5618

Oleskevich, D. A., Hyndman, R. D., & Wang, K. (1999). The updip and downdip limits to great subduction earthquakes: Thermal and structural models of Cascadia, South Alaska, SW Japan, and Chile. *Journal of Geophysical Research*, *104*(B7), 14965–14991. https://doi.org/10.1029/1999JB900060

Park, J., & Rye, D. M. (2019). Why is crustal underplating beneath many hotspot islands anisotropic? *Geochemistry, Geophysics, Geosystems*, *20*(11), 4779–4809. https://doi.org/10.1029/2019GC008492

Paulatto, M., Jiang, Y., Galve, A., Laigle, M., Rietbrock, A., Segovia, M., & Vaca, S. (2024). The effect of subduction relief on megathrust slip properties in Ecuador, constraints from gravity anomalies and seismic tomography. In *EGU general assembly 2024*.

Paulatto, M., Laigle, M., Galve, A., Charvis, P., Sapin, M., Bayrakci, G., et al. (2017). Dehydration of subducting slow-spread oceanic lithosphere in the Lesser Antilles. *Nature Communications*, *8*(1), 15980. https://doi.org/10.1038/ncomms15980

Ramos, M. D., Liberty, L. M., Haeussler, P. J., & Humphreys, R. (2022). Upper-plate structure and tsunamigenic faults near the Kodiak Islands, Alaska, USA. *Geosphere*, *18*(5), 1474–1491. https://doi.org/10.1130/GES02486.1

Reece, R. S., Gulick, S. P. S., Christeson, G. L., Horton, B. K., Van Avendonk, H., & Barth, G. (2013). The role of farfield tectonic stress in oceanic intraplate deformation, Gulf of Alaska. *Journal of Geophysical Research: Solid Earth*, *118*(5), 1862–1872. https://doi.org/10.1002/jgrb.50177

Reece, R. S., Gulick, S. P. S., Horton, B. K., Christeson, G. L., & Worthington, L. L. (2011). Tectonic and climatic influence on the evolution of the Surveyor Fan and Channel system, Gulf of Alaska. *Geosphere*, *7*(4), 830–844. https://doi.org/10.1130/GES00654.1

Richards, M., Contreras-Reyes, E., Lithgow-Bertelloni, C., Ghiorso, M., & Stixrude, L. (2013). Petrological interpretation of deep crustal intrusive bodies beneath oceanic hotspot provinces. *Geochemistry, Geophysics, Geosystems*, *14*(3), 604–619. https://doi.org/10.1029/2012GC004448

Robinson, D. P., Das, S., & Watts, A. B. (2006). Earthquake rupture stalled by a subducting fracture zone. *Science*, *312*(5777), 1203–1205. https://doi.org/10.1126/science.1125771

Roland, E., Lizarralde, D., McGuire, J. J., & Collins, J. A. (2012). Seismic velocity constraints on the material properties that control earthquake behavior at the Quebrada-Discovery-Gofar transform faults, East Pacific Rise. *Journal of Geophysical Research*, *117*(B11), B11102. https://doi.org/10.1029/2012JB009422

Ruff, L., & Kanamori, H. (1980). Seismicity and the subduction process. *Physics of the Earth and Planetary Interiors*, *23*(3), 240–252. https://doi.org/10.1016/0031-9201(80)90117-X

Ruff, L. J. (1989). Do trench sediments affect great earthquake occurrence in subduction zones? In L. J. Ruff, & H. Kanamori (Eds.), *Subduction zones part II* (pp. 263–282). Birkhäuser Basel. https://doi.org/10.1007/978-3-0348-9140-09

Ryan, H. F., von Huene, R., Wells, R. E., Scholl, D. W., Kirby, S., & Draut, A. E. (2012). *History of earthquakes and tsunamis along the eastern Aleutian-Alaska megathrust, with implications for tsunami hazards in the California continental borderland* (Vol. 1795, p. 31). U.S. Geological Survey Professional Paper. https://doi.org/10.3133/pp1795a

Ryan, W. B. F., Carbotte, S. M., Coplan, J. O., O'Hara, S., Melkonian, A., Arko, R., et al. (2009). Global multi-resolution topography synthesis. *Geochemistry, Geophysics, Geosystems*, *10*(3), Q03014. https://doi.org/10.1029/2008GC002332

Saffer, D. M., & Wallace, L. M. (2015). The frictional, hydrologic, metamorphic and thermal habitat of shallow slow earthquakes. *Nature Geoscience*, *8*(8), 594–600. https://doi.org/10.1038/ngeo2490

Sallarès, V., & Ranero, C. R. (2019). Upper-plate rigidity determines depth-varying rupture behaviour of megathrust earthquakes. *Nature*, *576*(7785), 96–101. https://doi.org/10.1038/s41586-019-1784-0

Sandwell, D. T., M̈ uller, R. D., Smith, W. H. F., Garcia, E., & Francis, R. (2014). New global marine gravity model from CryoSat-2 and Jason-1 reveals buried tectonic structure. *Science*, *346*(6205), 65–67. https://doi.org/10.1126/science.1258213

Scholl, D. W., Kirby, S. H., von Huene, R., Ryan, H., Wells, R. E., & Geist, E. L. (2015). Great (Mw8.0) megathrust earthquakes and the subduction of excess sediment and bathymetrically smooth seafloor. *Geosphere*, *11*(2), 236–265. https://doi.org/10.1130/GES01079.1

Scholz, C. H. (1998). Earthquakes and friction laws. *Nature*, *391*(6662), 37–42. https://doi.org/10.1038/34097

Shillington, D. (2011). Alaska Langseth experiment to understand the megaThrust [Dataset]. *International Federation of Digital Seismograph Networks*. https://doi.org/10.7914/SN/ZF_2011

Shillington, D. J., Bécel, A., & Nedimović, M. R. (2022). Upper plate structure and megathrust properties in the Shumagin gap near the July 2020 M7.8 Simeonof event. *Geophysical Research Letters*, *49*(2), e2021GL096974. https://doi.org/10.1029/2021GL096974

Shillington, D. J., Bécel, A., Nedimović, M. R., Kuehn, H., Webb, S. C., Abers, G. A., et al. (2015). Link between plate fabric, hydration and subduction zone seismicity in Alaska. *Nature Geoscience*, *8*(12), 961–964. https://doi.org/10.1038/ngeo2586

Silver, E. A., Ellis, M. J., Breen, N. A., & Shipley, T. H. (1985). Comments on the growth of accretionary wedges. *Geology*, *13*(1), 6–9. https://doi.org/10.1130/0091-7613(1985)13%3C6:COTGOA%3E2.0.CO;2

Singh, S. C., Hananto, N., Mukti, M., Robinson, D. P., Das, S., Chauhan, A., et al. (2011). Aseismic zone and earthquake segmentation associated with a deep subducted seamount in Sumatra. *Nature Geoscience*, *4*(5), 308–311. https://doi.org/10.1038/ngeo1119

Stevenson, A. J., Scholl, D. W., & Vallier, T. L. (1983). Tectonic and geologic implications of the Zodiac fan, Aleutian Abyssal Plain, northeast Pacific. *Geological Society of America Bulletin*, *94*(2), 259–273. https://doi.org/10.1130/0016-7606(1983)94%3C259:TAGIOT%3E2.0.CO;2

Suess, E., Bohrmann, G., von Huene, R., Linke, P., Wallmann, K., Lammers, S., et al. (1998). Fluid venting in the eastern Aleutian subduction zone. *Journal of Geophysical Research*, *103*(B2), 2597–2614. https://doi.org/10.1029/97JB02131

Suito, H., & Freymueller, J. T. (2009). A viscoelastic and afterslip postseismic deformation model for the 1964 Alaska earthquake. *Journal of Geophysical Research*, *114*(B11), B11404. https://doi.org/10.1029/2008JB005954

Suleimani, E., & Freymueller, J. T. (2020). Near-field modeling of the 1964 Alaska tsunami: The role of splay faults and horizontal displacements. *Journal of Geophysical Research: Solid Earth*, *125*(7), e2020JB019620. https://doi.org/10.1029/2020JB019620

Sun, T., Ellis, S., & Saffer, D. (2020). Coupled evolution of deformation, pore fluid pressure, and fluid flow in shallow subduction forearcs. *Journal of Geophysical Research: Solid Earth*, *125*(3), e2019JB019101. https://doi.org/10.1029/2019JB019101

Sykes, L. R., Kisslinger, J. B., House, L., Davies, J. N., & Jacob, K. H. (1981). Rupture zones and repeat times of great earthquakes along the Alaska-Aleutian arc, 1784–1980. In *Earthquake prediction* (pp. 73–80). American Geophysical Union (AGU). https://doi.org/10.1029/ME004p0073

Tsuji, T., Ashi, J., Strasser, M., & Kimura, G. (2015). Identification of the static backstop and its influence on the evolution of the accretionary prism in the Nankai Trough. *Earth and Planetary Science Letters*, *431*, 15–25. https://doi.org/10.1016/j.epsl.2015.09.011

Van Avendonk, H. J. A., Harding, A. J., Orcutt, J. A., & McClain, J. S. (1998). A two-dimensional tomographic study of the Clipperton transform fault. *Journal of Geophysical Research*, *103*(B8), 17885–17899. https://doi.org/10.1029/98JB00904

von Huene, R., Miller, J. J., & Dartnell, P. (2015). A possible transoceanic tsunami directed toward the U.S. west coast from the Semidi segment, Alaska convergent margin. *Geochemistry, Geophysics, Geosystems*, *17*(3), 645–659. https://doi.org/10.1002/2015GC006147

von Huene, R., Miller, J. J., & Krabbenhoeft, A. (2021). The Alaska convergent margin backstop splay fault zone, a potential large tsunami generator between the frontal prism and continental framework. *Geochemistry, Geophysics, Geosystems*, *22*(1), e2019GC008901. https://doi.org/10.1029/2019GC008901

von Huene, R., Miller, J. J., & Weinrebe, W. (2012). Subducting plate geology in three great earthquake ruptures of the western Alaska margin, Kodiak to Unimak. *Geosphere*, *8*(3), 628–644. https://doi.org/10.1130/GES00715.1

Wallace, L. M., Beavan, J., McCaffrey, R., & Darby, D. (2004). Subduction zone coupling and tectonic block rotations in the North Island, New Zealand. *Journal of Geophysical Research*, *109*(B12), B12406. https://doi.org/10.1029/2004JB003241

Wallace, L. M., Fagereng, Å., & Ellis, S. (2012). Upper plate tectonic stress state may influence interseismic coupling on subduction megathrusts. *Geology*, *40*(10), 895–898. https://doi.org/10.1130/G33373.1

Wang, F., Wei, S. S., Drooff, C., Elliott, J. L., Freymueller, J. T., Ruppert, N. A., & Zhang, H. (2024). Fluids control along-strike variations in the Alaska megathrust slip. *Earth and Planetary Science Letters*, *633*, 118655. https://doi.org/10.1016/j.epsl.2024.118655

Wang, K., & Bilek, S. L. (2011). Do subducting seamounts generate or stop large earthquakes? *Geology*, *39*(9), 819–822. https://doi.org/10.1130/G31856.1

Wang, K., & Bilek, S. L. (2014). Invited review paper: Fault creep caused by subduction of rough seafloor relief. *Tectonophysics*, *610*, 1–24. https://doi.org/10.1016/j.tecto.2013.11.024

Warwel, A., Lange, D., Dannowski, A., Wirp, S. A., Contreras-Reyes, E., Klaucke, I., et al. (2024). Structure and geometry of the Chilean subduction zone near Copiapó (27°S) based on an amphibious seismic refraction experiment. In *EGU general assembly 2024*.

Watt, J. T., & Brothers, D. S. (2020). Systematic characterization of morphotectonic variability along the Cascadia convergent margin: Implications for shallow megathrust behavior and tsunami hazards. *Geosphere*, *17*(1), 95–117. https://doi.org/10.1130/GES02178.1

Watts, A. B., Grevemeyer, I., Shillington, D. J., Dunn, R. A., Boston, B., & Gómez de la Peña, L. (2021). Seismic structure, gravity anomalies and flexure along the Emperor Seamount chain. *Journal of Geophysical Research: Solid Earth*, *126*(3), e2020JB021109. https://doi.org/10.1029/2020JB021109

Wei, S. S., Ruprecht, P., Gable, S. L., Huggins, E. G., Ruppert, N., Gao, L., & Zhang, H. (2021). Along-strike variations in intermediate-depth seismicity and arc magmatism along the Alaska Peninsula. *Earth and Planetary Science Letters*, *563*, 116878. https://doi.org/10.1016/j.epsl.2021.116878

Wessel, P., & Kroenke, L. W. (1998). The geometric relationship between hot spots and seamounts: Implications for pacific hot spots. *Earth and Planetary Science Letters*, *158*(1), 1–18. https://doi.org/10.1016/S0012-821X(98)00043-0

White, M. C., Fang, H., Nakata, N., & Ben-Zion, Y. (2020). PyKonal: A python package for solving the Eikonal equation in spherical and Cartesian coordinates using the fast marching method [Software]. *Seismological Research Letters*, *91*(4), 2378–2389. https://doi.org/10.1785/0220190318

Xiao, Z., Freymueller, J. T., Grapenthin, R., Elliott, J. L., Drooff, C., & Fusso, L. (2021). The deep Shumagin gap filled: Kinematic rupture model and slip budget analysis of the 2020 Mw 7.8 Simeonof earthquake constrained by GNSS, global seismic waveforms, and floating InSAR. *Earth and Planetary Science Letters*, *576*, 117241. https://doi.org/10.1016/j.epsl.2021.117241

Ye, L., Bai, Y., Si, D., Lay, T., Cheung, K. F., & Kanamori, H. (2022). Rupture model for the 29 July 2021 Mw 8.2 Chignik, Alaska earthquake constrained by seismic, geodetic, and tsunami observations. *Journal of Geophysical Research: Solid Earth*, *127*(7), e2021JB023676. https://doi.org/10.1029/2021JB023676

Ye, S., Flueh, E. R., Klaeschen, D., & von Huene, R. (1997). Crustal structure along the EDGE transect beneath the Kodiak shelf off Alaska derived from OBH seismic refraction data. *Geophysical Journal International*, *130*(2), 283–302. https://doi.org/10.1111/j.1365-246X.1997.tb05648.x

Zelt, C. A. (1998). Lateral velocity resolution from three-dimensional seismic refraction data. *Geophysical Journal International*, *135*(3), 1101–1112. https://doi.org/10.1046/j.1365-246X.1998.00695.x

Zhang, J., & Gulick, S. P. (2019). Sequence stratigraphy and depositional history of the Baranof Fan: Insights for Cordilleran Ice Sheet outflow to the Gulf of Alaska. *Geological Society of America Bulletin*, *132*(1–2), 353–372. https://doi.org/10.1130/B35164.1

References From the Supporting Information

Bassett, D., & Watts, A. B. (2015b). Gravity anomalies, crustal structure, and seismicity at subduction zones: 1. Seafloor roughness and subducting relief. *Geochemistry, Geophysics, Geosystems*, *16*(5), 1508–1540. https://doi.org/10.1002/2014GC005684

Fisher, M. A., Bruns, T. R., & von Huene, R. (1981). Transverse tectonic boundaries near Kodiak Island, Alaska. *Geological Society of America Bulletin*, *92*(1), 10–18. https://doi.org/10.1130/0016-7606(1981)92⟨10:TTBNKI⟩2.0.CO;2

Meléndez, A., Korenaga, J., Sallarès, V., Miniussi, A., & Ranero, C. (2015). TOMO3D: 3-D joint refraction and reflection traveltime tomography parallel code for active-source seismic data—Synthetic test. *Geophysical Journal International*, *203*(1), 158–174. https://doi.org/10.1093/gji/ggv292

U.S. Geological Survey, Bankey, V., Cuevas, A., Daniels, D. L., Finn, C. A., Hernandez, I., et al. (2002). Magnetic anomaly map of North America [Report]. https://doi.org/10.3133/70211067